Comparison of different data-assimilation approaches to augment RANS turbulence models

Arthur Shiniti Cato, Pedro Stefanin Volpiani, Vincent Mons, Olivier Marquet, Denis Sipp

Comparison of different data-assimilation approaches to augment RANS turbulence models

Arthur Shiniti Cato, Pedro Stefanin Volpiani,* Vincent Mons, Olivier Marquet, and Denis Sipp
ONERA, The French Aerospace Lab, 8 Rue de Vertugadins, 92190 Meudon, France
(Dated: August 28, 2023)

Reynolds-averaged Navier-Stokes (RANS) simulations are the most widespread approach to predict turbulent flows typical of industrial problems. Despite its success, the inherent simplifications and assumptions used to model the unknown Reynolds stresses are sources of inaccuracies. With this in mind, data-assimilation (DA) techniques can be used to minimize errors between the predicted and the exact flow fields by optimizing a space-dependent correction term. This correction term can be subsequently fed into machine learning algorithms to enhance RANS turbulence models. The main objective of this work is to assess the performance of several correction terms to match a full mean-flow velocity field, provided by averaged DNS simulations, and analyze the pros and cons of each when used subsequently in a machine-learning based RANS framework. Three configurations were chosen to perform the analysis: the converging-diverging channel at $Re = 12600$, the flow over periodic hills at $Re = 2800$, and the square cylinder at $Re = 22000$. Six different correction terms were considered and discussed in this paper. Assimilations based on eddy-viscosity corrections, albeit constrained by the Boussinesq hypothesis, were able to correct the velocity field even for flows exhibiting large recirculation regions. However, the precise choice of the correction term employed has a major impact in the optimization process. On the other hand, when correction is applied as source terms in the momentum equations, better fit of the corrected mean-flow field is achieved.

I. INTRODUCTION

Turbulence is one of the most intriguing problems in classical physics and it remains as a major subject of research until the present days. As a matter of fact, many questions related to turbulence are still open. Moreover, many applications in engineering rely on the prediction of turbulent flows, for instance: aircraft design, atmospheric flows, gas turbine engines, reactive flows etc. Despite the increase in computational power over the last decades, the full solution of Navier-Stokes equations remains unfeasible for the majority of applications. Therefore, engineers have to rely on turbulence models to overcome this challenge.

The most usual approach to predict turbulent flows is to consider the Reynolds averaged Navier-Stokes (RANS) equations, which is based on the Reynolds decomposition, involving the mean field (statistical ensemble average) and the fluctuation part. The Reynolds stress tensor, that accounts of the effect of the fluctuations on the mean flow, can be modeled as functions of the mean field variables in order to close the set of equations. It is remarkably cheaper to solve the RANS equations with a closure equation than a Direct Numerical Simulation (DNS); besides, as many applications require only the information of the mean field, this technique presents some advantages. On the other hand, the necessity of a model for the Reynolds stress tensor, which is usually designated as a closure model, makes it less accurate and arduous to describe the physics properly. Between these two methods, there is the Large Eddy Simulation (LES) in which the smallest scales of the flow are filtered and only the largest eddies are captured in the computational grid. This approach, although less expensive than the DNS, is still prohibitive in many cases; moreover, it still relies on turbulence modelling in the sense that the interaction between the small filtered scales and the non-filtered ones has to be modeled.

The great efforts to develop closure equations for the RANS equations resulted in several well-known models, for instance, the one-equation model Spalart-Almaras (SA) [1], the two-equation models $k-\epsilon$ [2] and $k-\omega$ [3], and their many variations. All these models have sets of parameters which are calibrated using experimental data from some simple canonical flows. As each model has been developed to suit a limited range of flows and their parameters seem to be non-universal, their accuracy and uncertainties are constantly being questioned (see discussion in [4]).

A more systematic methodology is used in the general framework of data-driven turbulence modelling in order to minimize the discrepancy between the data and the output of the model for a specific flow scenario. For instance, Li *et al.*[5] determined the coefficients of a $k-\omega$ model in order to minimize the velocity error with respect to high-fidelity simulations. The optimization problem can then be treated with, for example, gradient-based techniques or

*Electronic address: pedro.stefanin_volpiani@onera.fr

ensemble-based method. Unlike Li *et al.*[5], the technique used in the present work tries to address model-form errors instead of parametric ones. Unlike the traditional methods based on the inference of model parameters, the idea is to use a correction field varying in space which allows one to access solutions beyond the space solution of the original model. This freedom makes it possible to analyze model-form errors.

Data assimilation (DA) in field inversion problems can be found in several works in the scientific literature. In Foures *et al.* [6], data provided from a DNS simulation of a flow over a cylinder was used to tune the Reynolds stress term of the RANS equations in a way to reconstruct the flow. In Franceschini *et al.* [7], a data-assimilation procedure was used in the case of a backward-facing step at moderated Reynolds number to tune volumetric forces in the momentum equations and in the Spalart-Allmaras model. Li *et al.* [8] also studied the problem for other cases. Moreover, rather than additive correction terms in the models, other works considered multiplicative terms to correct the models, for instance, in Duraisamy *et al.* (2017)[9], data-assimilation with respect to a field $\beta(\mathbf{x})$, which multiplies the production term in the Spalart-Allmaras model, was considered. Other examples are found in [10], [11] and [12].

Data-assimilation related to the Spalart-Allmaras model presented promising results in many of the previous cited works, on the other hand, correction terms imposed on the turbulent model rather than the momentum equations remain constrained to the validity of the Boussinesq hypothesis. Franceschini *et al.*[7] addressed this challenge as the rigidity of the correction field. Their study evaluated the flexibility of several correction terms, in either the momentum or eddy-viscosity equations, to quantify their capability to reconstruct reference mean-flows according to the flow features, i.e., presence of large or thin recirculated region, geometry etc.

Another important motivation of the cited assimilation approach is the increasing use of machine-learning to enhance turbulence models over the last decade. A common technique is to use high-fidelity data to directly estimate a correction term to be learned. For instance, Wang *et al.*[13] used a technique based on random forest to reconstruct the discrepancy between the Reynolds stress in RANS simulations and DNS databases. In the same direction, Wu *et al.*[14] described a data-augmented turbulence framework in order to create a systematic machine-learning approach to learn the Reynolds stress tensor. Ling *et al.*[15] presented a method of deep neural network to reconstruct the Reynolds stress anisotropy tensor. Nevertheless, if input features are computed from DNS, the constructed field can be inconsistent with the RANS model structure. On top of that, this methodology can create an ill-conditioned problem when correcting directly the Reynolds stresses in the RANS framework (see [16, 17]). For this reason, Cruz et al. [18], Berrone and Oberto [19] proposed to work with the Reynolds force vector (the divergence of the Reynolds stress tensor) given by high-fidelity simulations as a target for the machine learning technique. Parish *et al.*[20] proposed a two-step procedure to avoid model inconsistency, namely field inversion and machine learning (FIML), where data-assimilation is performed to infer a model correction term and, then, machine-learning is done to generalize it. Although, under favorable circumstances, the direct acquisition of the correction term from experiments can provide reasonable results, the step addressing data-assimilation to compute the model correction terms, also known as field inversion, is important to guarantee the consistency with the model structure. Other works as Duraisamy *et al.* (2019)[21] and Duraisamy (2021)[22] discuss the state of the art of model-consistent machine-learning. In addition, FIML was applied in several recent studies: Köhler *et al.*[23] employed FIML on a $k-\epsilon$ model to reconstruct discrepancies in wall-bounded flows with separation and reattachment; Ferrero *et al.*[24] applied artificial neural network, using data from correction fields, to improve RANS-SA models for low pressure gas turbine cascades; and Rumsey *et al.*[25] worked on a wide variety of flows in the machine-learning step to enhance the SA model. These works used as modelling term the $\beta(\mathbf{x})$ field related to turbulence production. Additionally, Volpiani *et al.* (2021)[26] tuned a source term in the RANS momentum equations to correct the flow over periodic hills and trained a neural network with the data assimilated-fields to model the discrepancy between DNS and RANS.

Although several works dedicated to model the discrepancies between models and experiments through machine-learning exist, questions about how the inverse problem should be approached remain. Therefore, the main motivation of the present work is to compare the performance of different non-parametric control terms to solve the inverse problem of assimilation. As the properties and behaviours of these problems are often unknown, the aim is to pragmatically study the flexibility of the optimization procedure for different tuning terms to correct the baseline model, being constrained to the same computational meshes as the ones used for the RANS calculations, the same numerical methods and cost functional. The focus is directed to cases where the Spalart-Allmaras performs poorly, the Boussinesq hypotheses is questionable or/and the character of the flow is highly unsteady. Even for these cases, some of the control parameters can express surprising results as it is shown further. We apply the methodology presented here in three flow cases, in which the level of accuracy of the Boussinesq hypotheses is more or less respected.

This work is organized as follows: section II presents the mathematical formulation of the problem and the description of the method, which is based on a variational formulation to solve the optimization problem related to the data-assimilation method; section III discusses the results concerning the data-assimilation of the convergent-divergent channel with emphasis on the different performances of each control term used; section IV continues the investigation for the periodic hills flow case, characterized by a stronger separation and misalignment between the stress tensor and strain tensor; section V shows the results of the data-assimilation for the square cylinder flow case to illustrate

the performance of the method in a strongly separated flow and also highly unsteady; section VI summarizes the advantages and drawbacks of each control term employed to correct the model in the machine-learning framework; finally, the main conclusions are exposed.

II. METHODOLOGY

This section describes the method proposed to perform the data-assimilation. First (§II A), we present the reference and baseline predicted solutions. We consider the RANS-Spalart-Allmaras (SA) model, even though the methodology is not limited to this specific model and is rather general; the advantage of the SA model is its simplicity and broad application in industry, e.g., aviation. Then (§II B), the data-assimilation problem is described in the form of a deterministic optimization problem with various control parameters added to the baseline RANS-SA equations. The objective functional we aim to minimize is given by the discrepancy between the reconstructed and the reference velocity fields. After presenting in §II C the gradient of the objective with respect to the various control parameters and their properties, we briefly recall the optimization strategy in §II D and the elements of the numerical discretization in §II E.

A. Reference and baseline mean flows

The flow variables $\mathbf{q} = [\mathbf{u}, p]^T$ are separated into the sum of two components: the mean flow $\overline{\mathbf{q}} = [\overline{\mathbf{u}}, \overline{p}]^T$ and the fluctuations $\mathbf{q}' = [\mathbf{u}', p']^T$. The reference mean flow satisfies the steady incompressible RANS equations

$$\nabla \cdot \overline{\mathbf{u}} = 0, \tag{1a}$$

$$\overline{\mathbf{u}} \cdot \nabla \overline{\mathbf{u}} + \nabla \overline{p} - \nabla \cdot (\nu \nabla_s \overline{\mathbf{u}}) = -\nabla \cdot (\overline{\mathbf{u}' \otimes \mathbf{u}'}) \tag{1b}$$

where $\nabla_s = (\nabla + \nabla^T)$ is twice the symmetric component of the velocity gradient and $\overline{\mathbf{u}' \otimes \mathbf{u}'}$ is the Reynolds stress tensor. In the following, such reference data will be obtained from DNS data.

Using a turbulence model to close the above RANS equations, we obtain a predicted baseline mean flow $\tilde{\mathbf{q}} = [\tilde{\mathbf{u}}, \tilde{p}]^T$. Here we consider the classical Boussinesq approximation for the Reynolds stress tensor $-\overline{\mathbf{u}' \otimes \mathbf{u}'} = \nu_t \nabla_s \tilde{\mathbf{u}} - \frac{2}{3} k \mathbf{I}$, where ν_t is the eddy-viscosity and $k = \frac{1}{2}\left(\overline{u'}^2 + \overline{v'}^2 + \overline{w'}^2\right)$ is the turbulent kinetic energy, usually accounted in the pressure term.

We use the particular Spalart-Allmaras-neg one equation turbulence model introduced by Crivellini et al. [27]:

$$\nabla \cdot \tilde{\mathbf{u}} = 0, \tag{2a}$$

$$\tilde{\mathbf{u}} \cdot \nabla \tilde{\mathbf{u}} + \nabla \tilde{p} - \nabla \cdot (\nu \nabla_s \overline{\mathbf{u}}) = \nabla \cdot [\nu_t(\tilde{\nu}) \nabla_s \tilde{\mathbf{u}}], \tag{2b}$$

$$\tilde{\mathbf{u}} \cdot \nabla \tilde{\nu} - \nabla \cdot [\eta(\tilde{\nu}) \nabla \tilde{\nu}] = \underbrace{P(\tilde{\nu}, \nabla \tilde{\mathbf{u}}) - D(\tilde{\nu}, \nabla \tilde{\mathbf{u}}) + C(\nabla \tilde{\nu})}_{s(\tilde{\nu}, \nabla \tilde{\nu}, \nabla \tilde{\mathbf{u}})}, \tag{2c}$$

while the eddy-viscosity $\nu_t(\tilde{\nu})$ and diffusion coefficient $\eta(\tilde{\nu})$ are modelled as:

$$\nu_t(\tilde{\nu}) = \begin{cases} \tilde{\nu} f_{v1}, & \tilde{\nu} \geq 0 \\ 0, & \tilde{\nu} < 0 \end{cases}, \quad f_{v1} = \frac{\chi^3}{c_{v1}^3 + \chi^3}, \quad \chi = \frac{\tilde{\nu}}{\nu}, \quad \eta(\tilde{\nu}) = \begin{cases} \sigma^{-1} \nu (1 + \chi) & , \ \chi \geq 0 \\ \sigma^{-1} \nu \left(1 + \chi + \frac{1}{2}\chi^2\right) & , \ \chi < 0 \end{cases}. \tag{3}$$

The source term $s(\tilde{\nu}, \nabla \tilde{\nu}, \nabla \tilde{\mathbf{u}})$ is composed of a production, destruction and cross-diffusion term:

$$P(\tilde{\nu}, \nabla \overline{\mathbf{u}}) = \begin{cases} c_{b1} \tilde{\nu} \tilde{S} & , \ \chi \geq 0 \\ c_{b1} \tilde{\nu} S g_n & , \ \chi < 0 \end{cases}, \quad D(\tilde{\nu}, \nabla \overline{\mathbf{u}}) = \begin{cases} c_{w1} f_w \left(\frac{\tilde{\nu}}{d}\right)^2 & , \ \chi \geq 0 \\ -c_{w1} \left(\frac{\tilde{\nu}}{d}\right)^2 & , \ \chi < 0 \end{cases}, \quad C(\nabla \tilde{\nu}) = \frac{c_{b2}}{\sigma} \nabla \tilde{\nu} \cdot \nabla \tilde{\nu}, \tag{4}$$

where:

$$\begin{aligned} \tilde{S} &= S + \frac{\tilde{\nu} f_{v2}}{k^2 d^2}, \quad S = \sqrt{|\nabla \times \overline{\mathbf{u}}|^2 + M^2} - M, \quad f_{v2} = 1 - \frac{\chi}{1 + \chi f_{v1}}, \quad g_n = 1 - 1000 \frac{\chi^2}{1 + \chi^2}, \\ f_w &= g \left[\frac{1 + c_{w3}^6}{g^6 + c_{w3}^6}\right]^{\frac{1}{6}}, \quad g = r + c_{w2}\left(r^6 - r\right), \quad r = \begin{cases} r', & 0 \leqslant r' \leqslant 10, \\ 10, & r' < 0, r' > 10 \end{cases}, \quad r' = \frac{\tilde{\nu}}{\tilde{S} k^2 d^2}. \end{aligned}$$

Here d is the distance to the nearest wall, $c_{v1} = 7.1$, $c_{b1} = 0.1355$, $c_{b_2} = 0.622$, $\sigma = 2/3$, $k = 0.41$, $c_{w_1} = c_{b1}/k^2 + (1 + c_{b2})/\sigma$, $c_{w2} = 0.3$, $c_{w3} = 2$. We also introduced the regularizing constant $M = 10^{-5}$ to avoid differentiability issues of S.

B. Data assimilation framework

Six correction terms are considered in the governing equations (2):

$$\nabla \cdot \tilde{\mathbf{u}} = 0, \tag{5a}$$

$$\tilde{\mathbf{u}} \cdot \nabla \tilde{\mathbf{u}} + \nabla \tilde{p} - \nabla \cdot (\nu \nabla_s \tilde{\mathbf{u}}) = \nabla \cdot [(1+\xi)\, \nu_t(\tilde{\nu}) \nabla_s \tilde{\mathbf{u}} + \mathbf{R}_{\gamma\delta}] + \tilde{\mathbf{f}}_{\mathbf{u}}, \tag{5b}$$

$$\tilde{\mathbf{u}} \cdot \nabla \tilde{\nu} - \nabla \cdot [\eta(\tilde{\nu}) \nabla \tilde{\nu}] = (1+\beta)\, P(\tilde{\nu}, \nabla \tilde{\mathbf{u}}) - D(\tilde{\nu}, \nabla \tilde{\mathbf{u}}) + C(\nabla \tilde{\nu}) + \tilde{f}_{\tilde{\nu}} + \tilde{g}_{\tilde{\nu}} \tilde{\nu}. \tag{5c}$$

All these terms are space-dependent: $\tilde{\mathbf{f}}_{\mathbf{u}} := \tilde{\mathbf{f}}_{\mathbf{u}}(\mathbf{x})$, $\mathbf{R}_{\gamma\delta} := \mathbf{R}_{\gamma\delta}(\mathbf{x})$, $\tilde{f}_{\tilde{\nu}} := \tilde{f}_{\tilde{\nu}}(\mathbf{x})$, $\tilde{g}_{\tilde{\nu}} := \tilde{g}_{\tilde{\nu}}(\mathbf{x})$, $\beta := \beta(\mathbf{x})$, $\xi := \xi(\mathbf{x})$. These correctors are therefore non-parametric, i.e., they do not rely just in the tuning of numerical model coefficients, rather they allow the model to explore solutions which would be outside the original space of solutions (see [4]).

Parameters β, $\tilde{f}_{\tilde{\nu}}$ and $\tilde{g}_{\tilde{\nu}}$ are introduced in the equation governing the turbulence variable: the correction term β adjusts the production of turbulence-eddy viscosity, as proposed by Singh and Duraisamy [28], while parameters $\tilde{f}_{\tilde{\nu}}$ and $\tilde{g}_{\tilde{\nu}}$ fix the overall value of the source term. The effectiveness of the correction $\tilde{g}_{\tilde{\nu}}$ is conditioned by a non-zero value of the turbulence variable; hence its gradient is forced to be located in boundary layers or separated regions, which are physically meaningful regions for turbulence length-scale corrections. On the contrary, the gradient associated to the correction $\tilde{f}_{\tilde{\nu}}$ is generally located more upstream and may point even to non-physical regions (for example the uniform upstream flow region). This difference might have a strong impact on the efficiency of the optimization procedure [12]. Finally, ξ multiplies the eddy-viscosity in the momentum equation and intends to directly fix the eddy-viscosity value. All these parameters force the solution to be constrained within the Boussinesq hypothesis: only the length-scale of the turbulence is corrected, not the structure of the Reynolds-stresses, which remain aligned with the velocity gradient tensor.

On the other hand, parameters $\tilde{\mathbf{f}}_{\mathbf{u}}$ and $\mathbf{R}_{\gamma\delta}$ yield solutions that are not constrained by the Boussinesq hypothesis, and may therefore be considered as a cure to its limitations. The parameter $\mathbf{R}_{\gamma\delta} = \begin{pmatrix} \gamma & \delta \\ \delta & -\gamma \end{pmatrix}$ is taken as a trace-free symmetric tensor, standing for a conservative force, which is consistent with the fact that Reynolds stresses should be conservative. Note that the vector field (γ, δ) is defined up to a divergence-free potential flow, since $(\gamma + \partial_x \phi, \delta + \partial_y \phi)$ with $\partial_{xx}\phi + \partial_{yy}\phi = 0$ yields the same forcing as (γ, δ). This degree of freedom could in particular be used to enforce specific conditions on the full Reynolds stresses, for example realizability [29]. The correction term $\tilde{\mathbf{f}}_{\mathbf{u}}$ is in contrast not conservative in general.

A cost functional is then defined as the error between the computed velocity field of the model and the reference mean velocity field:

$$J(\tilde{\mathbf{u}}) = \frac{1}{2} \int_\Omega \|\tilde{\mathbf{u}} - \overline{\mathbf{u}}\|^2 \, d\Omega, \tag{6}$$

where $\langle \mathbf{a}, \mathbf{b} \rangle_\Omega = \int_\Omega \mathbf{a} \cdot \mathbf{b} \;\; d\Omega$. The cost functional J is then minimized constrained to the governing equations. All optimizations are performed with a single parameter, i.e. the various parameters introduced above are considered one at a time.

If the cost-functional reaches a zero value, the full reconstructed Reynolds stress vector on the right-hand-side of eq. (5b),

$$\mathbf{f}^{DA} = \nabla \cdot [(1+\xi)\, \nu_t(\tilde{\nu}) \nabla_s \tilde{\mathbf{u}} + \mathbf{R}_{\gamma\delta}] + \tilde{\mathbf{f}}_{\mathbf{u}}, \tag{7}$$

should match $\tilde{\mathbf{u}} \cdot \nabla \tilde{\mathbf{u}} + \nabla \tilde{p} - \nabla \cdot (\nu \nabla_s \tilde{\mathbf{u}})$, with $\tilde{\mathbf{u}} = \overline{\mathbf{u}}$ and $\tilde{\mathbf{p}} = \overline{\mathbf{p}} + \frac{2}{3}k$. Hence, the quantity

$$\mathbf{f}^{DNS} = -\nabla \cdot (\overline{\mathbf{u}' \otimes \mathbf{u}'}) + \frac{2}{3} \nabla k, \tag{8}$$

should accurately recover $\mathbf{f}^{DA}$. In Foures et al. [6], it was checked that the rotational of the Reynolds stress forces (which removes the potential part) perfectly agrees in such an ideal situation. In the following, we will however show that, due to the extreme sensitivity of the relation $\mathbf{f}^{DA} \to \tilde{\mathbf{u}}$, even minute discrepancies between $\tilde{\mathbf{u}}$ and $\overline{\mathbf{u}}$ will trigger noticeable differences between the two Reynolds stress forces. Note finally that matching the Reynolds stress forces does not induce matching the Reynolds stresses. Indeed, as already mentioned, a trace-free tensor characterized by two fields (γ, δ) yields the same force as any other trace-free tensor characterized by $(\gamma + \partial_x \phi, \delta + \partial_y \phi$ as soon as $\partial_{xx}\phi + \partial_{yy}\phi = 0$. Hence, in the absence of any additional knowledge of the Reynolds stresses (in particular if the objective functional only involves mean-flow velocity quantities), there is no reason a priori that the reconstructed Reynolds stresses $\mathbf{R}^{DA}$ and reference stresses $\mathbf{R}^{DNS}$, respectively defined as

$$\mathbf{R}^{DA} = (1+\xi)\, \nu_t(\tilde{\nu}) \nabla_s \tilde{\mathbf{u}} + \mathbf{R}_{\gamma\delta}, \quad \mathbf{R}^{DNS} = -\nabla \cdot (\overline{\mathbf{u}' \otimes \mathbf{u}'}) + \frac{2}{3} k \mathbf{I} \tag{9}$$

should match. This is a point that will also be illustrated in the following sections.

C. Objective functional gradients

The equivalent unconstrained problem can be written through the Lagrangian L, which is constructed with the help of Lagrange multipliers or adjoint variables $\tilde{\mathbf{u}}^\dagger$, $\tilde{p}^\dagger$ and $\tilde{\nu}^\dagger$. The Lagrangian can be written as

$$\begin{aligned} &L\left(\left[\tilde{\mathbf{u}},\tilde{p},\tilde{\nu}\right],\left[\tilde{\mathbf{u}}^\dagger,\tilde{p}^\dagger,\tilde{\nu}^\dagger\right],\left[\tilde{\mathbf{f}}_{\mathbf{u}},\tilde{f}_{\tilde{\nu}},\beta,\xi,\mathbf{R}_{\gamma\delta},\tilde{g}_{\tilde{\nu}}\right]\right) \\ &=J(\tilde{\mathbf{u}})+\langle\tilde{\mathbf{u}}^\dagger,\tilde{\mathbf{u}}\cdot\nabla\tilde{\mathbf{u}}+\nabla\tilde{p}-\nabla\cdot\left[\left(\nu+(1+\xi)\,\nu_t(\tilde{\nu})\right)\nabla_s\tilde{\mathbf{u}}+\mathbf{R}_{\gamma\delta}\right]-\tilde{\mathbf{f}}_{\mathbf{u}}\rangle_\Omega+\langle\tilde{p}^\dagger,\nabla\cdot\tilde{\mathbf{u}}\rangle_\Omega \\ &+\langle\tilde{\nu}^\dagger,\tilde{\mathbf{u}}\cdot\nabla\tilde{\nu}-\nabla\cdot\left(\eta(\tilde{\nu})\nabla\tilde{\nu}\right)-(1+\beta)\,P(\tilde{\nu},\nabla\tilde{\mathbf{u}})+D(\tilde{\nu},\nabla\tilde{\mathbf{u}})-C(\nabla\tilde{\nu})-\tilde{f}_{\tilde{\nu}}-\tilde{g}_{\tilde{\nu}}\tilde{\nu}\rangle_\Omega. \end{aligned} \tag{10}$$

The governing equations for the adjoint state are obtained by setting the variation of the Lagrangian with respect to the direct state to zero. The adjoint equations correspond to the following set of linear forced equations (see Appendix §A):

$$\nabla\cdot\tilde{\mathbf{u}}^\dagger=0, \tag{11a}$$

$$\tilde{\mathbf{u}}^\dagger\cdot(\nabla\tilde{\mathbf{u}})^T-\tilde{\mathbf{u}}\cdot\nabla\tilde{\mathbf{u}}^\dagger-\nabla\cdot\left[\left(\nu+(1+\xi)\nu_t\right)\nabla_s\tilde{\mathbf{u}}^\dagger\right]-\nabla\tilde{p}^\dagger+\tilde{\nu}^\dagger\nabla\tilde{\nu}+\nabla\cdot\left(\tilde{\nu}^\dagger\partial_{\nabla\tilde{u}}s\right)=-(\tilde{\mathbf{u}}-\overline{\mathbf{u}}) \tag{11b}$$

$$-\tilde{\mathbf{u}}\cdot\nabla\tilde{\nu}^\dagger-\nabla\cdot\left(\eta\nabla\tilde{\nu}^\dagger\right)+\left(\partial_{\tilde{\nu}}\eta\right)\nabla\tilde{\nu}^\dagger\cdot\nabla\tilde{\nu}+(1+\xi)\left(\partial_{\tilde{\nu}}\nu_t\right)\nabla\tilde{\mathbf{u}}^\dagger:\nabla_s\tilde{\mathbf{u}}-\left(\partial_{\tilde{\nu}}s\right)\tilde{\nu}^\dagger+\nabla\cdot\left(\tilde{\nu}^\dagger\partial_{\nabla\tilde{\nu}}s\right)-\tilde{g}_{\tilde{\nu}}\tilde{\nu}^\dagger=0, \tag{11c}$$

where it is seen that the forcing term is the discrepancy between the actual and reference solutions $\tilde{\mathbf{u}}-\overline{\mathbf{u}}$.

The variation of the Lagrangian with respect to each of the control terms gives the gradients:

$$\nabla_{\tilde{f}_{\mathrm{u}}}J=-\tilde{\mathbf{u}}^\dagger,\quad \nabla_{\mathbf{R}_{\gamma\delta}}J=\nabla\tilde{\mathbf{u}}^\dagger, \tag{12a}$$

$$\nabla_\xi J=\nu_t(\tilde{\nu})\nabla\tilde{\mathbf{u}}^\dagger:\nabla_s\tilde{\mathbf{u}},\quad \nabla_\beta J=-P(\tilde{\nu},\nabla\tilde{\mathbf{u}})\tilde{\nu}^\dagger,\quad \nabla_{\tilde{g}_{\tilde{\nu}}}J=-\tilde{\nu}\tilde{\nu}^\dagger.\quad \nabla_{\tilde{f}_{\tilde{\nu}}}J=-\tilde{\nu}^\dagger, \tag{12b}$$

The expression of these gradients yields some qualitative information on the location of the various control parameters. For example, it is seen that $\tilde{g}_{\tilde{\nu}}$ (resp. β) is located in the overlap region of $\tilde{\nu}$ (resp. $P(\tilde{\nu},\nabla\tilde{\mathbf{u}})$) and $\tilde{\nu}^\dagger$, while $\tilde{f}_{\tilde{\nu}}$ is located more upstream in the region where $\tilde{\nu}^\dagger$ is maximal. Hence, the $\tilde{f}_{\tilde{\nu}}$ control parameter may induce difficulties for the optimization algorithm to find the nonlinear optimum since this control parameter will be searched within a non-physical upstream region, where Reynolds stresses are weak. On the contrary, the parameter $\tilde{g}_{\tilde{\nu}}$ will be searched for in a viscous region characterized by non-zero values of $\tilde{\nu}$, which makes physical sense. Finally, the gradients involving derivative quantities of the direct and / or adjoint quantities, such as $\nabla_{\mathbf{R}_{\gamma\delta}}J$ or $\nabla_\xi J$, might be noisier. These remarks will help understand some of the observations made below.

Although the adjoint equations were derived within the continuous framework, we pick a discrete adjoint approach whenever possible to improve robustness. For example, the linear operator within (11) is simply obtained by a transpose of the discrete linearized governing equations, while the explicit expressions of the gradients are taken from the continuous framework within (12). The quality of the gradients has been checked against finite differences in appendix B.

D. Optimization algorithm

We consider the data-assimilation procedure introduced by Franceschini et al. [7] to optimize a given control parameter α (see Figure 1). We use the Low memory BroydenFletcherGoldfarbShanno (L-BFGS) implemented in the open library *scipy* in *Python* to perform the nonlinear optimization. It is a gradient based-method (requiring $\nabla_\alpha J$), which approximates the Hessian in an iterative way to evaluate the optimal parameter updates $\delta\alpha$ at each iteration. Note that the gradients being defined with respect to the scalar-product $\langle\mathbf{a},\mathbf{b}\rangle_\Omega$, a change of variable has to be applied to comply with the present L-BFGS implementation, which is restricted to Euclidian inner-products. More details can be found in Franceschini et al. [7]. Also, we have shown in appendix B a typical optimization history of the various gradient norms to assess the quality of the optimization procedures.

E. Spatial discretization and steady-state solver

The set of equations (5) is solved with a Finite Element Method (FEM) based on continuous Lagrange polynomials, within the *FreeFEM++* open-source software [30]. Such a FEM becomes numerically unstable for high Reynolds

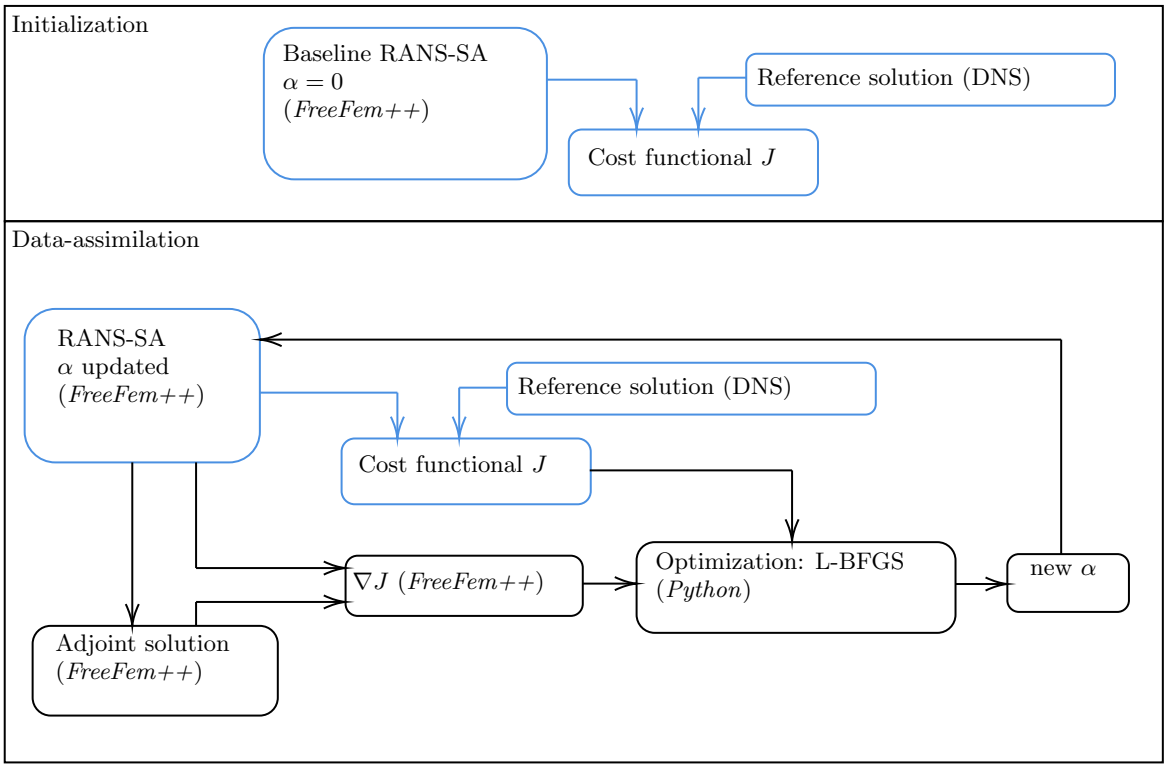

FIG. 1: Diagram of data-assimilation. Blue color identifies where the initialization is positioned in the data-assimilation loop. The letter α represents the general control parameter being tuned.

flows, thus a stabilization scheme is necessary. Following the works of Bao *et al.* (2011)[31], we chose to use the simplified version of the Streamline-Upwind Petrov-Galerkin (SUPG) scheme[32]. Consequently, only the advection terms are treated in this formulation. The weak form of equations 5 yields the following residual to be minmized[7]:

$$N\left([\tilde{\mathbf{u}},\tilde{p},\tilde{\nu}],[\tilde{\mathbf{v}},\tilde{q},\hat{\nu}]\right) = \int_\Omega (\tilde{\mathbf{u}}\cdot\nabla\tilde{\mathbf{u}})\cdot\tilde{\mathbf{v}}d\Omega + \int_\Omega \left(-\tilde{p}I + (\nu+\nu_t)\nabla_s\tilde{\mathbf{u}}\right):\nabla\tilde{\mathbf{v}}d\Omega - \int_\Omega (\nabla\cdot\tilde{\mathbf{u}})\,\tilde{q}d\Omega \tag{13}$$

$$+ \int_\Omega (\tilde{\mathbf{u}}\cdot\nabla\tilde{\nu} - s)\,\hat{\nu}d\Omega + \int_\Omega \eta\nabla\tilde{\nu}\cdot\nabla\hat{\nu}d\Omega \tag{14}$$

$$+ \sum_{\Omega_k}\int_{\Omega_k} \tau_{SUPG}\tilde{\mathbf{u}}\cdot\nabla\tilde{\mathbf{v}}\,(\tilde{\mathbf{u}}\cdot\nabla\tilde{\mathbf{u}})\,d\Omega_k + \sum_{\Omega_k}\int_{\Omega_k}\tau_{SUPG}\tilde{\mathbf{u}}\cdot\nabla\hat{\nu}\,(\tilde{\mathbf{u}}\cdot\nabla\tilde{\nu})\,d\Omega_k, \tag{15}$$

where the function τ_{SUPG} is given as:

$$\tau_{SUPG} = \frac{f(Re_h)h_T}{2|\mathbf{u}|}, \quad f(Re_h) = \begin{cases} \frac{Re_h}{3}, & Re_h \leqslant 3 \\ 1, & Re_h > 3 \end{cases}, \quad Re_h = \frac{|\mathbf{u}|h_T}{2\nu}. \tag{16}$$

The local Reynolds number Re_h is defined based on the local element size $h_T = \sqrt{2}A/h_T^{max}$. Briefly, the aim is to find $[\tilde{\mathbf{u}},\tilde{p},\tilde{\nu}]$ such that for $\forall\,[\tilde{\mathbf{v}},\tilde{q},\hat{\nu}]$ and appropriate boundary conditions, we have $N\left([\tilde{\mathbf{u}},\tilde{p},\tilde{\nu}],[\tilde{\mathbf{v}},\tilde{q},\hat{\nu}]\right) = 0$. The nonlinear problem is solved with a Newton algorithm and the resulting large sparse systems of linear algebraic equations are solved based on the the Multifrontal Massively Parallel Sparse Direct Solver (MUMPS)[33, 34]. We use $\mathcal{P}_b^1$ elements for the velocity, and $\mathcal{P}^1$ elements for the pressure and eddy-viscosity fields, which results in a first-order accurate scheme. Baseline meshes were constructed taking into account the wall refinement of the DNS cases, ensuring mesh sizes below $y^+ = 1$ close to the walls. On top of that, a grid convergence study was performed for all configurations.

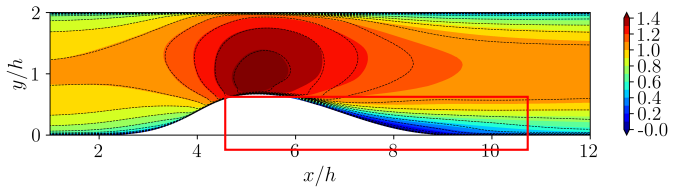

(a) RANS-SA horizontal velocity field $\tilde{u}/U_{ref}$.

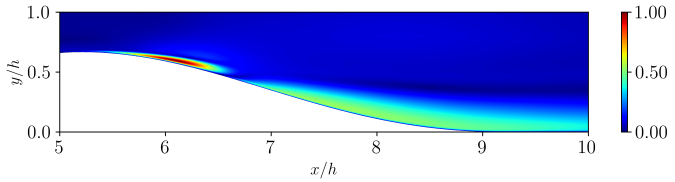

(b) Error field $e_{\tilde{\mathbf{u}}}/U_{ref}$

FIG. 2: Velocity field (u-component) of baseline RANS-SA, and the dotted lines represent level curves corresponding to the DNS field for comparison. Normalized error field based on equation 17. Red box indicates zone where discrepancies are highest, see figure (b).

III. CONVERGING-DIVERGING CHANNEL

A. Reference and base flows

We consider the converging-diverging channel at $Re = 12600$ (based on the inlet reference velocity) available within the public database in the *Turbulence Modelling Resource* from the *Langley Research Center*. Experimental tests were conducted in the wind tunnel of the *Laboratoire de Mécanique de Lille* by Bernard *et al.*[35] and Direct Numerical Simulations were done based on the same geometry (see [36] and [37]). The bump geometry was firstly designed to model an airfoil subjected to an adverse pressure gradient (APG) but sufficiently weak preventing the boundary layer from separating for the Reynolds number of the experiments. However, DNS computations ([36], [37]) showed a narrow region of re-circulation for the Reynolds numbers chosen. The works from Marquillie *et al.* (2008) [36] and Marquillie *et al.* (2011) [37] detail the main characteristics of the flow. The geometry can be found in other papers in the literature ([38], [39]). In the following, the inlet (resp. outlet) boundary condition is located at $x/h = 0$ (resp. $x/h = 12.5$), while the top-wall is at $y/h = 2$. The reference velocity scale U_{ref} is taken as the velocity at $(x/h = 0, y/h = 1)$.

The baseline SA solution is illustrated in Figure 2a. The inlet velocity profile is set using the DNS results with $\tilde{\nu}$ reconstructed from the turbulent stresses. While the upstream part of the bump is characterized by a favorable pressure gradient, its diverging part is dominated by an APG. The error field (Fig.2b) computed as

$$e_{\tilde{\mathbf{u}}}(\mathbf{x}) = \left[\left(\tilde{u}(\mathbf{x}) - \overline{u}(\mathbf{x}) \right)^2 + \left(\tilde{v}(\mathbf{x}) - \overline{v}(\mathbf{x}) \right)^2 \right]^{\frac{1}{2}}, \tag{17}$$

shows where the DNS and RANS-SA strongly disagree, i.e., the region downstream of the separation. Although the area characterized by the boundary separation seems to be rather small in the DNS, it is a challenging flow to be evaluated with the RANS-SA equations due to the thin elongated re-circulation and high-velocity gradients. The separation point predicted by the RANS computation is displaced downstream and the boundary layer does not seem to reattach until the final portion of the channel. Failing to reproduce the position of separation and reattachment of the boundary layer for this type of flow will impact the evaluation of quantities of interest such as the skin-friction or the pressure distribution.

B. Assimilated mean fields

The results of the data-assimilation concerning the $\tilde{\mathbf{f}}_{\mathbf{u}}$, $\mathbf{R}_{\gamma\delta}$, β, $\tilde{f}_{\tilde{\nu}}$, $\tilde{g}_{\tilde{\nu}}$ and ξ terms are now presented. The data-assimilation procedure based on the momentum forcing $\tilde{\mathbf{f}}_{\mathbf{u}}$ and conservative momentum forcing $\mathbf{R}_{\gamma\delta}$ are less constrained than the ones that modify the value of the eddy-viscosity field ν_t. The cost functional decreased almost three orders of magnitude (see Figure 3) for the terms that directly affect the momentum equation. Nevertheless, the overall velocity

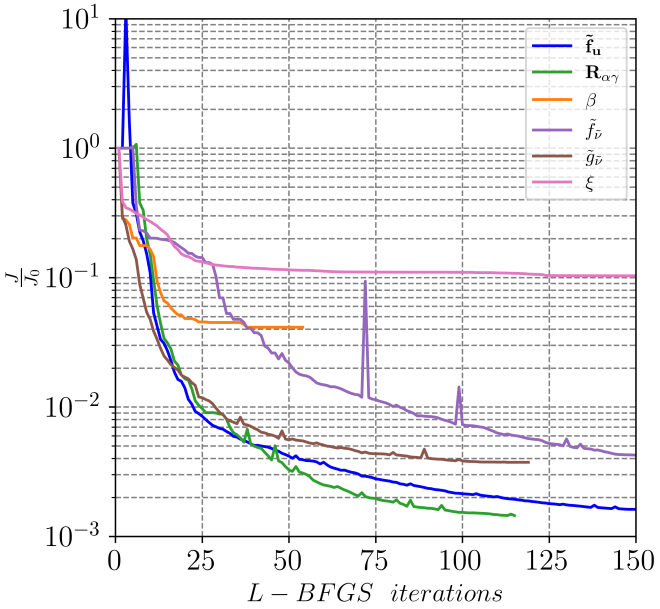

FIG. 3: Cost functional during data-assimilation iterations.

TABLE I: C_f error computed as $E_{Cf} = \sqrt{\int (C_f^{DA/RANS} - C_f^{DNS})^2 ds / \int (C_f^{DNS})^2 ds}$ and final relative velocity error $E_{\tilde{\mathbf{u}}} = \sqrt{\iint e_{\tilde{\mathbf{u}}}^2 d\Omega / \iint U_{ref}^2 d\Omega}$ for each reconstructed field.

	RANS	$\tilde{\mathbf{f}}_\mathbf{u}$	$\mathbf{R}_{\gamma\delta}$	β	$\tilde{f}_{\tilde{\nu}}$	$\tilde{g}_{\tilde{\nu}}$	ξ
E_{Cf}	0.39	0.059	0.057	0.18	0.19	0.12	0.23
$E_{\tilde{\mathbf{u}}}$	$4.9 \cdot 10^{-2}$	$3.1 \cdot 10^{-3}$	$2.9 \cdot 10^{-3}$	$8.4 \cdot 10^{-3}$	$8.1 \cdot 10^{-3}$	$4.6 \cdot 10^{-3}$	$1.2 \cdot 10^{-2}$

fields corrected with β, $\tilde{f}_{\tilde{\nu}}$ and $\tilde{g}_{\tilde{\nu}}$ were also greatly improved. Although the ξ term had the lowest performance, the overall reconstruction is still reasonable. These conclusions are illustrated by the reconstructed velocity profiles with three correction terms ($\tilde{\mathbf{f}}_\mathbf{u}$, $\tilde{g}_{\tilde{\nu}}$ and ξ) in Figure 4. General profiles related to $\mathbf{R}_{\gamma\delta}$, β and $\tilde{f}_{\tilde{\nu}}$ (not shown) were similar to $\tilde{\mathbf{f}}_\mathbf{u}$ and $\tilde{g}_{\tilde{\nu}}$.

The u^+ profiles (Figures 4b and 4c) as well as the skin friction coefficient C_f (Figure 5) were considered to assess the quality of the reconstruction close to the wall. The dimensionless velocity profiles were computed in two ways: i) considering the DNS shear stress as reference scale (Figure 4b), i.e., $u_\tau = \sqrt{\tau_w^{DNS}/\rho}$, and ii) considering each assimilated shear stress as the reference scale (Figure 4c), i.e., $u_\tau = \sqrt{\tau_w^{DA/RANS}/\rho}$. The first case confirms the improvement of the velocity profiles both close to the wall and in the bulk as the curves collapse using the same shear velocity. However, we reveal more of the differences between the reconstructed fields if we use the corresponding assimilated shear velocity as reference. These differences are reflected in the streamwise shear stress distribution, shown in Figure 5. The fact that J represents an L_2-norm of the error in the velocity field makes the assimilation of the whole domain prioritized over the correction of small or localized regions, e.g., very close to the wall.

The values of each $C_f = 2u_\tau^2/U_{ref}^2$ were integrated along the wall and compared to the base flow. They are presented in table I jointly with the final cost functional achieved with the algorithm. We notice a similarity between the C_f and J reduction for the cases $\tilde{\mathbf{f}}_\mathbf{u}$ and $\mathbf{R}_{\gamma\delta}$; as well as $\tilde{f}_{\tilde{\nu}}$ and $\tilde{g}_{\tilde{\nu}}$. The similarities are expected, at certain level, due to the fact that these terms are related.

The norm of the gradients are presented in Appendix §B to verify if a local minimum was approached and the capability of the algorithm to find a descent direction. It was found that the ξ correction rapidly interrupts the L-BFGS iterations. Furthermore, the optimization problem related to ξ can be ill-conditioned as discussed in [40] and this fact is evidenced in the form of small perturbations of the assimilated field in the separated region (see Figure 5f); this conclusion is in agreement with [40].

In figure 6, we compare the eddy viscosity obtained via different DA procedures, the original SA model and an

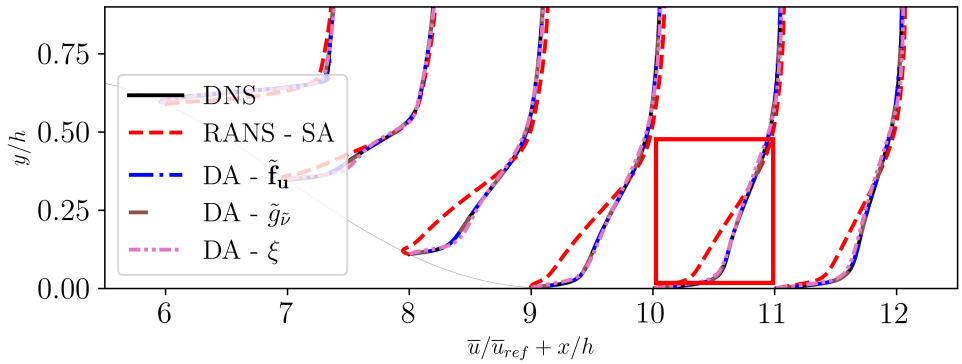

(a) Velocity profiles of the RANS-SA, DNS and assimilated solutions for $\tilde{\mathbf{f}}_\mathbf{u}$, $\tilde{g}_{\tilde{\nu}}$ and ξ.

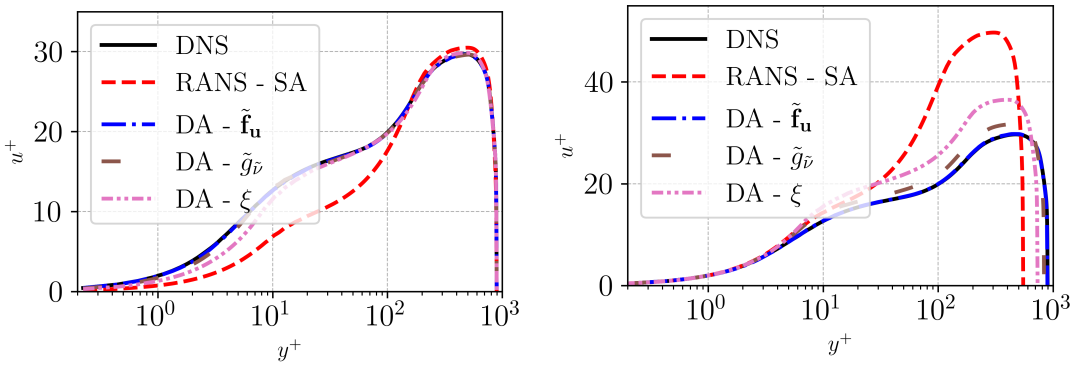

(b) u^+ and y^+ at $\frac{x}{h} = 10$. Shear velocity computed as $u_\tau = \sqrt{\tau_w^{DNS}/\rho}$.

(c) u^+ and y^+ at $\frac{x}{h} = 10$. Shear velocity computed as $u_\tau = \sqrt{\tau_w^{DA/RANS/DNS}/\rho}$

FIG. 4: Velocity (u-component) profiles of the assimilated solutions and DNS; red box indicates the approximated region at $\frac{x}{h} = 10$ where u^+ and y^+ were traced.

estimation from the DNS. The estimated ν_t obtained from the DNS solution was computed using the mean velocity fields and the components of the Reynolds stress tensor, as done in [41]:

$$\nu_t = \frac{\mathbf{R}^{DNS} : \nabla_s \overline{\mathbf{u}}}{\nabla_s \overline{\mathbf{u}} : \nabla_s \overline{\mathbf{u}}}, \tag{18}$$

where the notation $\mathbf{R}_1 : \mathbf{R}_2$ designates the double contraction between two tensors. Note that equation (18) remains an approximation and injecting the resulting turbulence viscosity in a RANS equation does not guarantee a perfect mean field. Nevertheless, it remains a good approximation for attached flows [41]. The baseline SA simulation mimics with a good accuracy the reference turbulence viscosity, but it presents lower values after the obstacle and on the top wall. The β-correction increases the production of ν_t and, consequently, the eddy viscosity attains higher values in this same region. Quantities based on $\tilde{f}_{\tilde{\nu}}$ and $\tilde{g}_{\tilde{\nu}}$ are also modified in the incoming boundary layer and in the top wall region. Since $\tilde{f}_{\tilde{\nu}}$ and $\tilde{g}_{\tilde{\nu}}$ are less spatially constrained than β (which is restricted to turbulent production regions), the ν_t values for the former cases are more scattered in the full separated region. Yet, the resulting eddy viscosity strongly differs from the expected one (for example, for the $\tilde{g}_{\tilde{\nu}}$-correction, the eddy viscosity reaches very high values in the central region of the channel after the bump), even though the assimilated mean-velocity results match the DNS with an excellent accuracy. The eddy viscosity computed using the ξ-parameter, $(1 + \xi)\nu_t$, is pretty much in agreement with the one predicted by the DNS, indicating that the DA managed to improve the original field and that it found a local minimum. For this case, we observe a noisy behavior in the eddy-viscosity field, especially where the flow separates, which can harm the optimization procedure and create numerical issues. Close to the walls, there is an important disagreement in the skin-friction profile between RANS-SA and DNS and all DA procedures manage to minimize this discrepancy.

Overall, $\tilde{g}_{\tilde{\nu}}$, $\tilde{f}_{\tilde{\nu}}$ and β recover very accurately the reference mean-velocity fields. Yet, it seems that this is at the expense of large eddy-viscosity corrections, which very strongly overshoot the reference values. Hence, we may be in

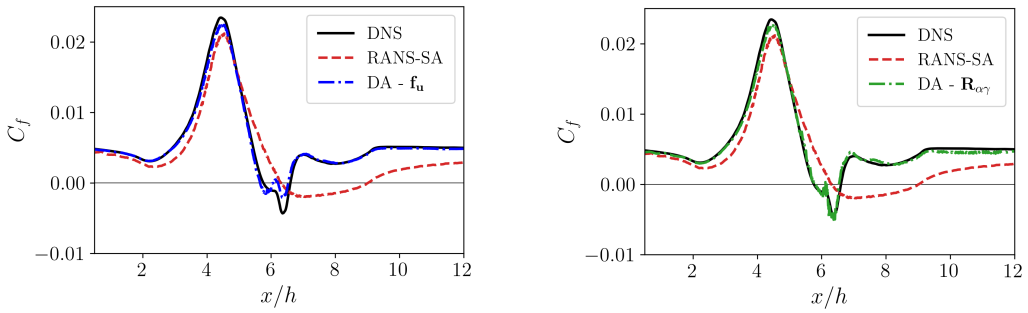

(a) Assimilation with $\tilde{\mathbf{f}}_{\mathbf{u}}$

(b) Assimilation with $\mathbf{R}_{\gamma\delta}$

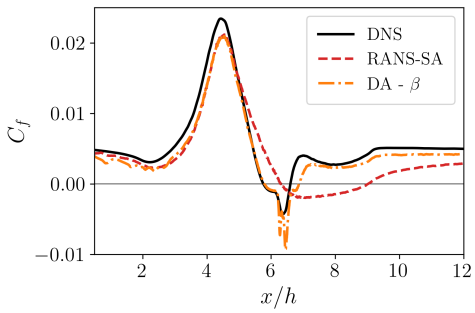

(c) Assimilation with β

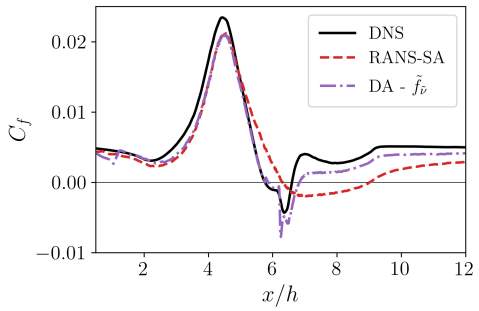

(d) Assimilation with $\tilde{f}_{\tilde{\nu}}$

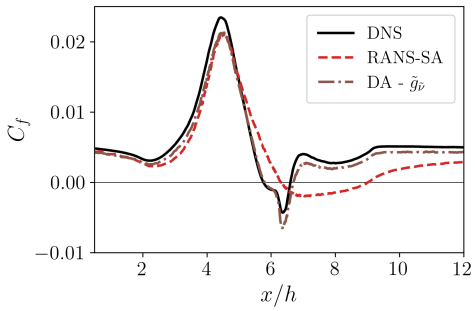

(e) Assimilation with $\tilde{g}_{\tilde{\nu}}$

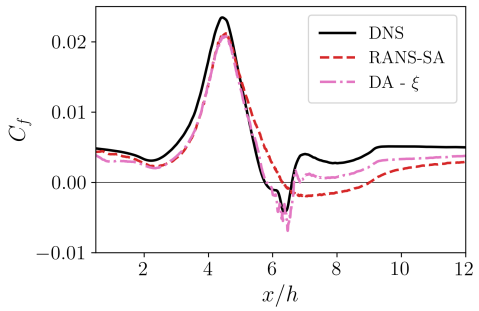

(f) Assimilation with ξ

FIG. 5: C_f of the assimilated solutions, DNS reference and the baseline RANS-SA. Black lines correspond to the DNS, dashed red lines correspond to the RANS-SA, dash-dotted colored lines correspond to the assimilated solutions

the case of a classical over-learning situation and a sole criterion on the mean-flow recovery may be insufficient to reach a good optimum. For example, penalizing the cost-functional J with a constraint on the norm of the control parameter, e.g.

$$J^{new}(\tilde{\mathbf{u}}, \tilde{g}_{\tilde{\nu}}) = J(\tilde{\mathbf{u}}) + l^2 \int_\Omega \tilde{g}_{\tilde{\nu}}^2 \, d\Omega, \tag{19}$$

or a constraint to remain close to a prior in ν_t, e.g.

$$J^{new}(\tilde{\mathbf{u}}, \tilde{\nu}) = J(\tilde{\mathbf{u}}) + l^2 \int_\Omega \left(\nu_t(\tilde{\nu}) - \nu_t^{RANS}\right)^2 d\Omega, \tag{20}$$

could help balance, by tuning the parameter l^2, the dual requirement to both accurately recover the mean velocity field and preserve a physical relevance of the control parameter (or the eddy-viscosity field). This double requirement

is very important especially if the control parameters are further used as data in a machine-learning strategy to correct the turbulcence model (see §VI). It seems that the ξ parameter reaches such a good compromise without penalizing term since both the velocity field and the eddy viscosity field are overall good at the end of the optimisation.

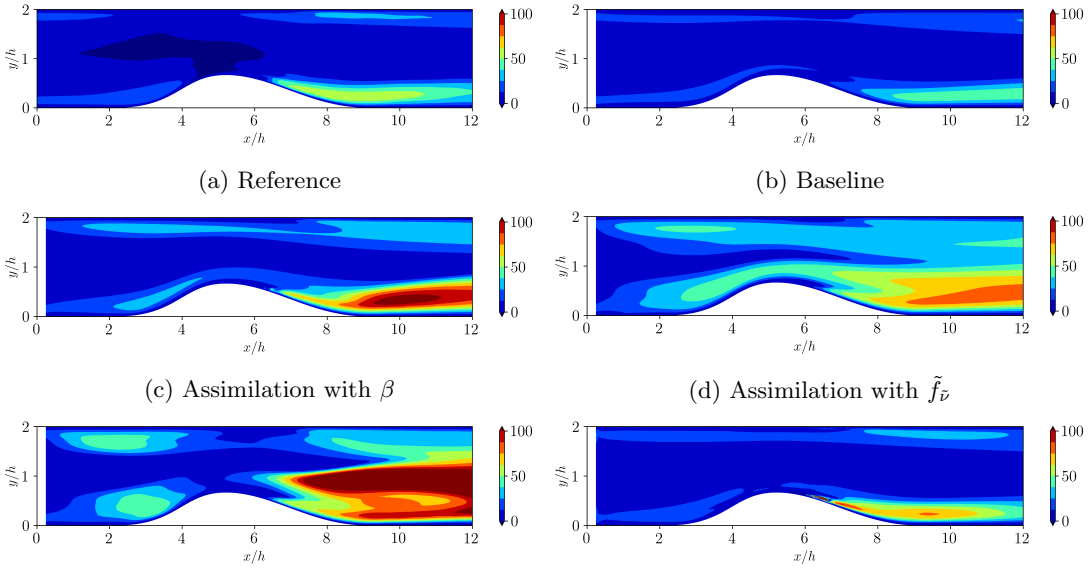

(a) Reference (b) Baseline

(c) Assimilation with β (d) Assimilation with $\tilde{f}_{\tilde{\nu}}$

(e) Assimilation with $\tilde{g}_{\tilde{\nu}}$ (f) Assimilation with ξ

FIG. 6: Distribution of ν_t/ν for the DNS, RANS - SA and assimilated fields. For the ξ-correction, the field represented is $(1+\xi)\,\frac{\nu_t}{\nu}$.

C. Validity of the Boussinesq hypotheses

We may discuss the alignment between the anisotropic stress tensor and the strain tensor, which is the basic idea of the Boussinesq hypothesis. In other words, given the anisotropic stress tensor $\mathbf{R}$ and the strain tensor $\nabla_s\mathbf{u}$, one can define ρ_{RS} as

$$\rho_{RS} = \frac{|\mathbf{R} : \nabla_s\mathbf{u}|}{\|\mathbf{R}\|\|\nabla_s\mathbf{u}\|} \tag{21}$$

where the norm $\|\cdot\|$ is defined as $\|\mathbf{R}\|^2 = \mathbf{R} : \mathbf{R}$.

In the work of Schmitt (2007)[42], the indicator ρ_{RS} is used to test the Boussinesq hypotheses. If ρ_{RS} is 1, it means that the tensors $\mathbf{R}$ and $\nabla_s\mathbf{u}$ are aligned and the Boussinesq hypothesis is totally respected, if it is 0, the tensors are orthogonal. In Schmitt (2007) [42], ρ_{RS} above 0.86 is considered to be good enough to assume the validity of the Boussinesq hypothesis. Figure 7 shows the values of ρ_{RS} in regions where turbulence is sufficiently strong. In other words, the velocity fluctuations can be very small in low turbulent regions and ρ_{RS} may be meaningless or deprecated[42] in these zones. Thus, Figure 7 is constrained to the regions where the turbulent kinetic energy is more important ($k > 0.1k_{max}$). Considering only regions where turbulence intensity is important, the ρ_{RS} values behind the hill very close to the wall (where reverse flow occurs) is below 0.8. This may indicate that the Boussinesq hypothesis is not adequate to predict the flow close to that region. However, the data-assimilation with $\tilde{g}_{\tilde{\nu}}$ was particularly robust to reconstruct this area (Figure 5e). A case where the alignment between the strain tensor and the anisotropic Reynolds stress may be clearly weak is presented next.

IV. PERIODIC HILLS

A. Reference and base flows

The flow over periodic hills has been extensively explored to study numerical methods and turbulence modelling (e.g. [43],[44],[45]). Thanks to the availability of high-fidelity data ([46],[47]), it is possible to test and compare

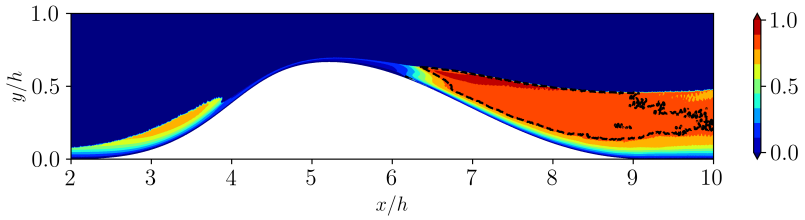

FIG. 7: Distribution of the indicator ρ_{RS} constrained to turbulent kinetic energy above 10% of k_{max}, i.e., $\rho^*_{\mathrm{RS}} = \rho_{\mathrm{RS}}$ for $k > 0.1k_{max}$ and $\rho^*_{\mathrm{RS}} = 0$ otherwise. Dashed line represents $\rho^*_{\mathrm{RS}} = 0.8$. Result computed from the reference DNS data.

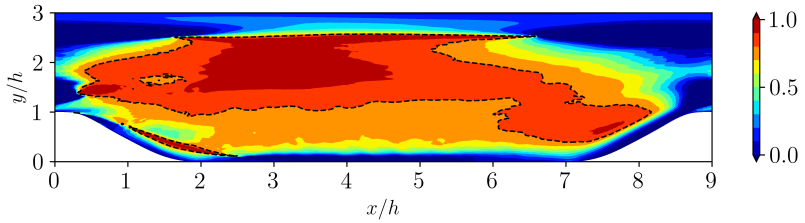

FIG. 8: Distribution of the indicator ρ_{RS}. Dashed line represents $\rho^*_{\mathrm{RS}} = 0.8$. Result computed from the reference DNS data.

different data-assimilation techniques. We consider the case where the bulk Reynolds number equals 2800. This case presents a curved geometry with a strong recirculating bubble. Flow separation occurs at the crest and the reattachment point is located at the flat surface. One main difference from the convergent-divergent channel is the intensity of the recirculation bubble and the strong unsteady dynamics associated to the large-scale eddies observed in the separated shear-layer containing most of the energy [45]. Additionally, the Boussinesq hypotheses is highly questioned for the periodic-hill case; the alignment between the stress tensor and the strain tensor measured by ρ_{RS} is less than 0.8 in much of the domain below $y/h = 1$, where separation occurs (Figure 8).

B. Assimilated mean fields

Similarly to the previous case, the decrease of J showed in Fig. 9 may indicate that the velocity fields resulting from $\tilde{\mathbf{f}}_{\mathbf{u}}$ and $\mathbf{R}_{\gamma\delta}$ corrections match the DNS better. Surprisingly, in spite of being constrained to the Boussinesq hypothesis, the terms $\tilde{f}_{\tilde{\nu}}$ and $\tilde{g}_{\tilde{\nu}}$ were also able to recover the overall DNS velocity profiles (not shown). The skin friction showed in Fig. 10 confirms that even close to the walls, the velocity gradients were significantly improved by correcting the eddy-viscosity model. The $\tilde{g}_{\tilde{\nu}}$ correction presents faster decay in the cost functional compared to $\tilde{f}_{\tilde{\nu}}$. The same conclusion was traced for the convergent-divergent channel. Notwithstanding, the correction through the production control β and ξ were not as effective (Figs. 10c and 10f) and it seems to be rather limited to decrease the cost functional compared to $\tilde{f}_{\tilde{\nu}}$ and $\tilde{g}_{\tilde{\nu}}$ (Fig. 9). The fact that $\tilde{g}_{\tilde{\nu}}$ and $\tilde{f}_{\tilde{\nu}}$ do so well despite their use of the Boussinesq hypothesis seems to indicate that missing the proper stress alignment does not play a large role for predicting the mean flow, even for this case where the stress misalignment is quite large.

Table II shows the final values of the relative velocity error and the relative error of C_f. The values are overall greater than the ones found in the convergent-divergent channel which seems reasonable due to the higher complexity of the flow. Moreover, the differences in the evolution of J for each correction approach are more evident. For the cases presented, it seems that $\tilde{\mathbf{f}}_{\mathbf{u}}$ and $\mathbf{R}_{\gamma\delta}$ corrections followed by $\tilde{g}_{\tilde{\nu}}$ and $\tilde{f}_{\tilde{\nu}}$ present more flexibility to reconstruct the DNS flow.

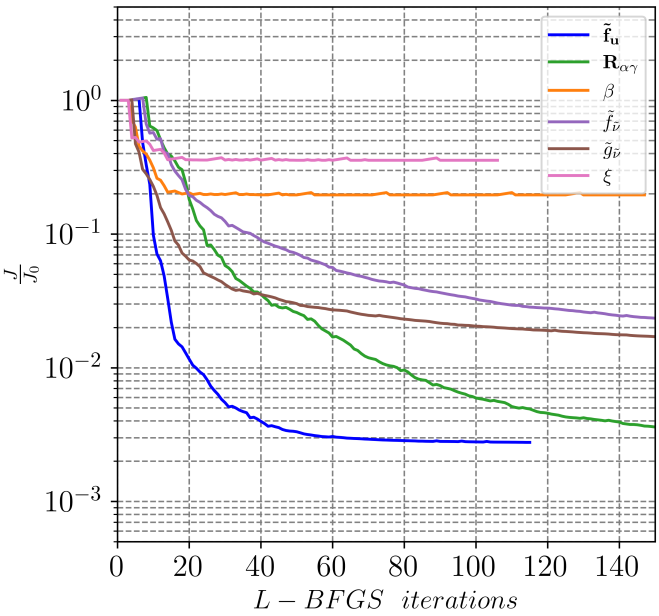

FIG. 9: Cost functional during data-assimilation iterations for the periodic hill flow.

TABLE II: C_f error computed as $E_{Cf} = \sqrt{\int (C_f^{DA/RANS} - C_f^{DNS})^2 ds / \int (C_f^{DNS})^2 ds}$ and final relative velocity error $E_{\tilde{\mathbf{u}}} = \sqrt{\iint e_{\tilde{\mathbf{u}}}^2 d\Omega / \iint U_{ref}^2 d\Omega}$ for each reconstructed field. Periodic hills case.

	RANS	$\tilde{\mathbf{f}}_{\mathbf{u}}$	$\mathbf{R}_{\gamma\delta}$	β	$\tilde{f}_{\tilde{\nu}}$	$\tilde{g}_{\tilde{\nu}}$	ξ
E_{Cf}	0.38	0.17	0.26	0.27	0.23	0.20	0.30
$E_{\tilde{\mathbf{u}}}$	$7.1 \cdot 10^{-2}$	$3.8 \cdot 10^{-3}$	$3.7 \cdot 10^{-3}$	$3.2 \cdot 10^{-2}$	$7.8 \cdot 10^{-3}$	$7.5 \cdot 10^{-3}$	$4.3 \cdot 10^{-2}$

V. SQUARE CYLINDER FLOW

A. Reference and base flows

The third case of study concerns the turbulent flow around a square cylinder at $Re = 22000$. Differently from the circular cylinder, the separation on the square cylinder is imposed by the corners of the square for sufficient high Reynolds numbers. This canonical configuration has been studied both experimentally and numerically [48]. Two of the main challenges for steady-state RANS modelling of this configuration are: capturing the highly unsteady (vortex shedding) character of the flow (without resorting to unsteady RANS computations) and the weakness of the Boussinesq hypothesis assumed in the RANS model. Figure 11 compares both the steady RANS and DNS solutions. One major difference between both results (RANS and DNS) is the size of the separation bubble downstream the cylinder. The aim of this section is to apply our assimilation approach to a bluff body configuration.

To understand the limitation of the Boussinesq hypotheses, the ρ_{RS} indicator is plotted in figure 12. Similarly to the conclusion traced in Schmitt (2007)[42], the region where the Boussinesq hypotheses is acceptable ($\rho_{RS} > 0.8$) is restricted to a few areas, with the indicator remaining unacceptably low (below the threshold) in most of the flow region.

B. Assimilated mean fields

The horizontal component of the assimilated velocity and the absolute error fields are compared in Figures 13 and 14 respectively. Figures 14b and 14c, which correspond to the $\tilde{\mathbf{f}}_{\mathbf{u}}$ and $\mathbf{R}_{\gamma\delta}$ corrections, show that both choices of correction parameters successfully reproduce the DNS simulation. As discussed before, it is reasonable to believe that they can perform corrections even in more complex flows. For this reason, Volpiani *et al.*(2021) [26] employed the

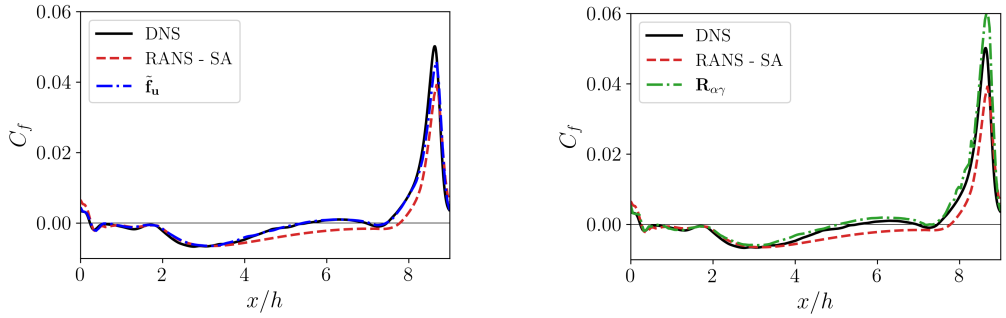

(a) Assimilation with $\tilde{\mathbf{f}}_\mathbf{u}$

(b) Assimilation with $\mathbf{R}_{\gamma\delta}$

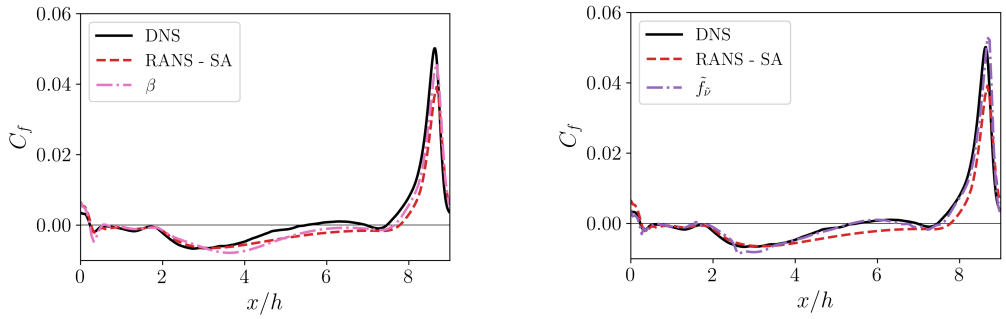

(c) Assimilation with β

(d) Assimilation with $\tilde{f}_{\tilde{\nu}}$

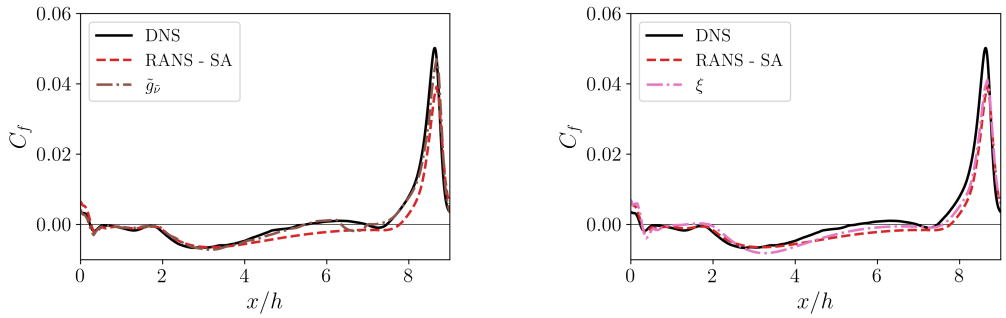

(e) Assimilation with $\tilde{g}_{\tilde{\nu}}$

(f) Assimilation with ξ

FIG. 10: C_f of the assimilated solutions, DNS reference and the baseline RANS-SA. Black lines correspond to the DNS, dashed red lines correspond to the RANS-SA, dash-dotted colored lines correspond to the assimilated solutions

$\tilde{\mathbf{f}}_\mathbf{u}$-type correction to construct a machine-learning based model for flows over periodic hills. The $\mathbf{R}_{\gamma\delta}$ corrector also managed to do the assimilation. This is an encouraging result and it reinforces that $\mathbf{R}_{\gamma\delta}$ can perform similarly to $\tilde{\mathbf{f}}_\mathbf{u}$, however the results for $\mathbf{R}_{\gamma\delta}$ were slightly noisier. It is possible that these deviations could have been originated due to numerical errors; for example, the gradient of the cost functional w.r.t. $\mathbf{R}_{\gamma\delta}$ may add rounding errors, once it needs additional information of the adjoint velocities spatial derivatives, which is not required in the $\tilde{\mathbf{f}}_\mathbf{u}$ correction.

The assimilated fields with β and $\tilde{f}_{\tilde{\nu}}$ are similar. Yet, before, the latter one provided better corrections than the former one, now, the opposite occurs here. Both fields improve the solution, decreasing the re-circulation bubble and approaching to the DNS simulation. The greatest portion of the velocity error in Fig. 14 is located in the recirculation zone, thus, the optimization problem is concentrated in reducing the discrepancy of the flow there. For case $\tilde{f}_{\tilde{\nu}}$, the optimization seems to follow this path even though the shear flow above the cylinder is deteriorated (Figure 14e). The initial decrease of the cost functional is then associated to the correction of the bubble and, after that, the shear flow over the cylinder gains importance regarding the L_2 norm employed. The reconstruction of this zone seems to be

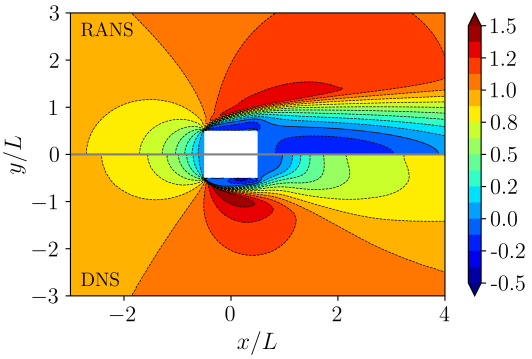

FIG. 11: Velocity fields (u-component) of the baseline RANS-SA, positive y-axis, compared to the DNS, negative y-axis. Full black lines delimit the bubble of re-circulation. The coordinates are normalized by the side L of the square cylinder.

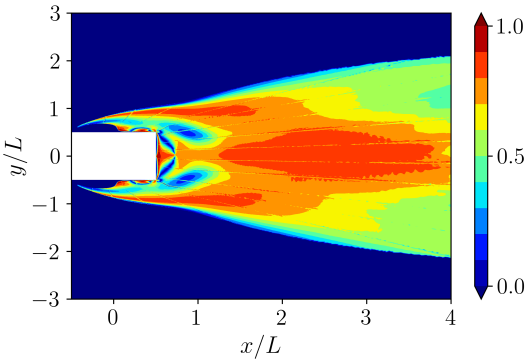

FIG. 12: Distribution of the indicator ρ_{RS} constrained to turbulent kinetic energy above 10% of k_{max}, i.e., $\rho^*_{\mathrm{RS}} = \rho_{\mathrm{RS}}$ for $k > 0.1k_{max}$ and $\rho^*_{\mathrm{RS}} = 0$ otherwise. Result computed from the reference DNS data.

more complicated. Note that even when averaging, the flow is still poorly predicted there[49]. Notwithstanding, the correction with $\tilde{g}_{\tilde{\nu}}$ was surprisingly effective and it performed almost as well as the source terms in the momentum equations.

The ξ approach was not able to correct the field, even though the re-circulation zone has decreased (figure 13f). *A priori*, the ξ control parameter was expected to perform similarly to β and $\tilde{f}_{\tilde{\nu}}$ but, from both the channel and the cylinder studies, it does not seem to be the case. In fact, the data-assimilation through terms directly placed on the Spalart-Allmaras model showed better robustness. To quantify the performance of each assimilation, Fig. 15 shows the cost functional decrease throughout the optimization procedure.

C. Discussion about assimilated and real quantities

Even if the assimilated fields can be overall similar to the DNS one, some quantities computed from the velocity fields can be very sensitive even to small differences or poorly predicted in the new flow. An evaluation *a posteriori* can be made using the assimilated fields to reconstruct other quantities. As evoked in [26], it is valuable to compare the stresses originated from the eddy-viscosity model with the reference from the DNS.

The components $\mathbf{R}^{DNS}$ of the traceless Reynolds stress tensor defined in (9) can be directly obtained by processing the DNS solution. They can be compared to the reconstructed stresses $\mathbf{R}^{DA}$ obtained from the RANS base flow or the data-assimilated flows and also defined in (9). Figures 16 and 17 compare the components R_{11} and R_{12} for several cases. We notice that the computed stress for the baseline SA result is very weak compared to the DNS. The data assimilation increases the overall magnitude of the stresses, however it is clear that they do not match exactly the reference DNS, even for the fields with great decrease of the cost functional (as case $\mathbf{R}_{\gamma\delta}$). Other evident problem is the stress distribution close to the corners of the cylinder, particularly for the cases $\mathbf{R}_{\gamma\delta}$ and $\tilde{g}_{\tilde{\nu}}$. Although an accurate velocity reconstruction in these regions, the recovered stresses are wrong. It is therefore confirmed that, in

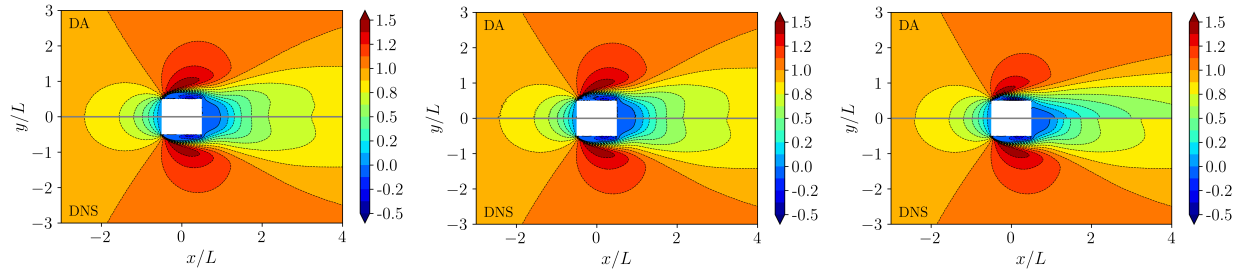

(a) Assimilation with $\tilde{\mathbf{f}}_{\mathbf{u}}$ (b) Assimilation with $\mathbf{R}_{\gamma\delta}$ (c) Assimilation with β

(d) Assimilation with $\tilde{f}_{\tilde{\nu}}$ (e) Assimilation with $\tilde{g}_{\tilde{\nu}}$ (f) Assimilation with ξ

FIG. 13: Velocity fields (u-component) of the assimilated fields (positive y-axis) compared to the DNS (negative y-axis). The coordinates are normalized by the side L of the square cylinder.

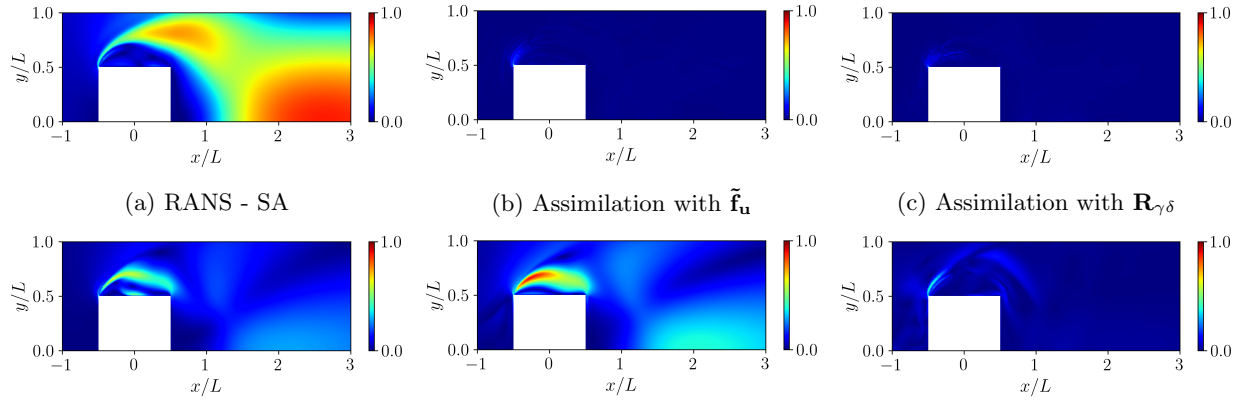

(a) RANS - SA (b) Assimilation with $\tilde{\mathbf{f}}_{\mathbf{u}}$ (c) Assimilation with $\mathbf{R}_{\gamma\delta}$

(d) Assimilation with β (e) Assimilation with $\tilde{f}_{\tilde{\nu}}$ (f) Assimilation with $\tilde{g}_{\tilde{\nu}}$

FIG. 14: Error of RANS and reconstructed velocity fields for $\tilde{\mathbf{f}}_{\mathbf{u}}$,$\mathbf{R}_{\gamma\delta}$, β, $\tilde{f}_{\tilde{\nu}}$ and $\tilde{g}_{\tilde{\nu}}$.

the absence of any knowledge from the reference Reynolds stresses, the mean-flow prediction can be accurate even though the Reynolds stresses are wrong. Nevertheless, some assimilations produced interesting results, for example, the R_{12} stress component for β, $\tilde{f}_{\tilde{\nu}}$ and $\tilde{g}_{\tilde{\nu}}$ seems to have greatly improved close to the cylinder. Overall, the $\tilde{g}_{\tilde{\nu}}$ correction not only improves the velocity field, but also manages to capture a realistic stress tensor especially in the wake region. Note finally that for the $\mathbf{R}_{\gamma\delta}$ reconstructions, we have to keep in mind that the stresses (γ, δ) are reconstructed up to a potential vector field $(\gamma + \partial_x\phi, \delta + \partial_y\phi)$, with $\partial_{xx}\phi + \partial_{yy}\phi = 0$, as mentioned in §II B. This degree of freedom could be used to improve the Reynolds stress reconstructions. For example, the knowledge of the Reynolds stresses in some region of the flow could be incorporated in the objective functional to precisely reconstruct the stresses.

For completeness, we also plot the full Reynolds force vector from the DNS, $\mathbf{f}^{DNS}$ defined in (8), and the reconstructed one $\mathbf{f}^{DA}$, defined in (7) in figures 18 and 19. Figure 18 shows the horizontal components f_x^{DNS}, f_x^{DA} and Figure 19 shows the vertical components f_y^{DNS}, f_y^{DA}. Firstly, we observe that the force vector given by the baseline SA model misrepresents the exact quantity computed from the DNS. This is of course expected given the mis-prediction of the solution for this test case. For case $\tilde{\mathbf{f}}_{\mathbf{u}}$, we note that the total force has a good accuracy in the shear and

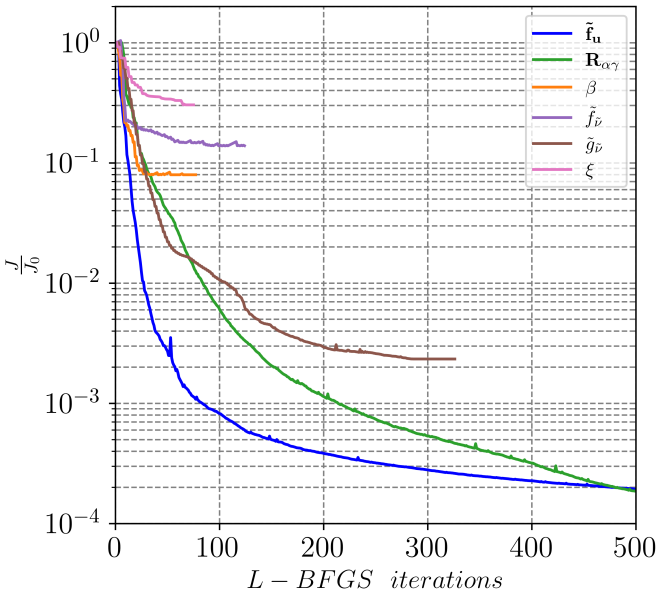

FIG. 15: Cost functional during data-assimilation iterations for the square cylinder flow.

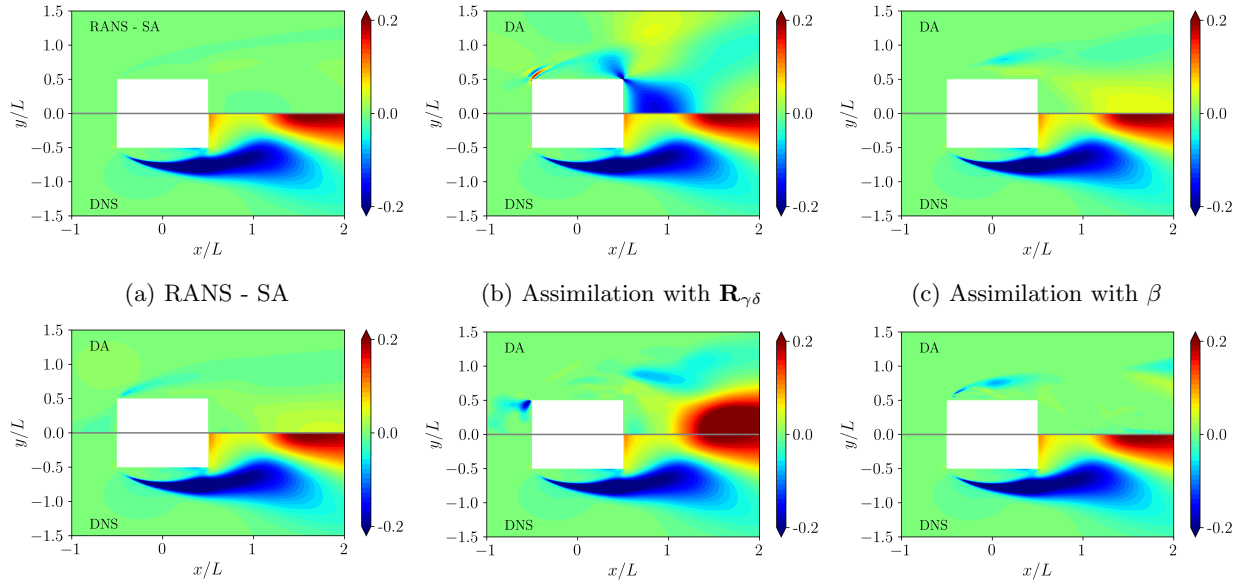

(a) RANS - SA (b) Assimilation with $\mathbf{R}_{\gamma\delta}$ (c) Assimilation with β

(d) Assimilation with $\tilde{f}_{\tilde{\nu}}$ (e) Assimilation with $\tilde{g}_{\tilde{\nu}}$ (f) Assimilation with ξ

FIG. 16: R_{11} component of the trace-less Reynolds stress tensor for RANS-SA, $\mathbf{R}_{\gamma\delta}$, β, $\tilde{f}_{\tilde{\nu}}$ and $\tilde{g}_{\tilde{\nu}}$

wake regions if we consider the most dominant component (f_x^{DA}), but it lacks accuracy in the other direction (f_y^{DA}). Despite the fact that the assimilation based on $\mathbf{R}_{\gamma\delta}$ does not give the correct stresses, it captures reasonably well the horizontal force f_x^{DA}. This indicates that even with the wrong stresses, it is possible to have accurate mean fields, as long as the Reynolds force vector is correctly represented. Concerning the correction included in the SA transport equation, both parameters β and $\tilde{f}_{\tilde{\nu}}$ give similar predictions and approach the reference data. On the other hand, the forcing fields resulting from the DA based on $\tilde{g}_{\tilde{\nu}}$ approximates better the DNS solution in the recirculation region, thanks to the good stress prediction. This is particularly interesting due to the fact that the correction was not simply able to approximate the DNS velocity field but also the stresses and forces in the wake region.

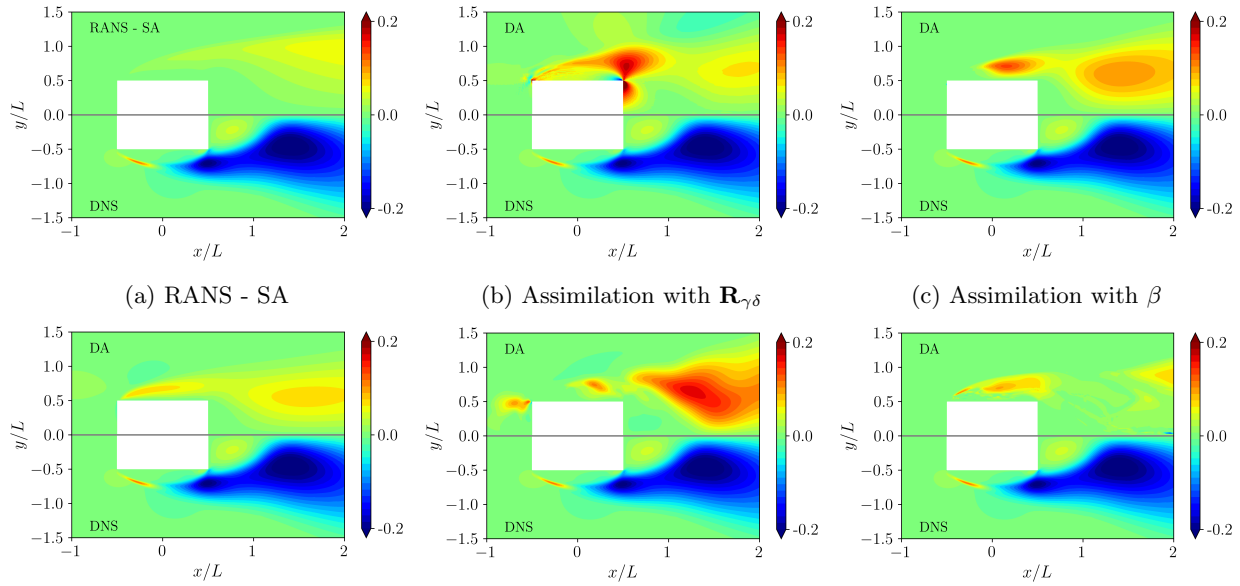

(a) RANS - SA (b) Assimilation with $\mathbf{R}_{\gamma\delta}$ (c) Assimilation with β

(d) Assimilation with $\tilde{f}_{\tilde{\nu}}$ (e) Assimilation with $\tilde{g}_{\tilde{\nu}}$ (f) Assimilation with ξ

FIG. 17: R_{12} component of the trace-less Reynolds stress tensor for RANS-SA, $\mathbf{R}_{\gamma\delta}$, β, $\tilde{f}_{\tilde{\nu}}$ and $\tilde{g}_{\tilde{\nu}}$

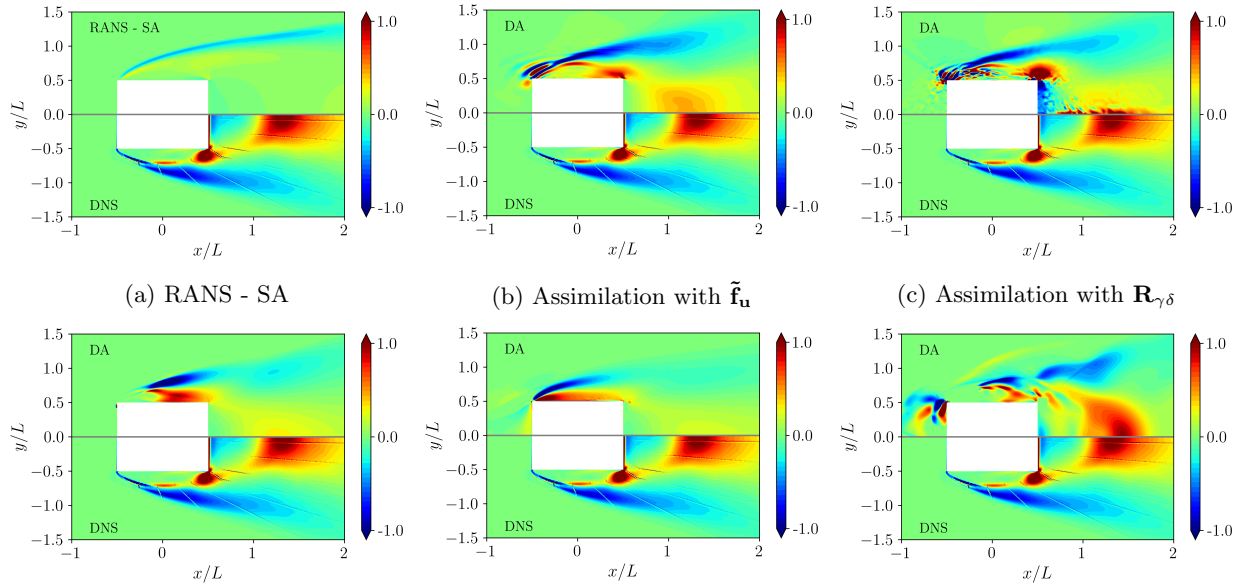

(a) RANS - SA (b) Assimilation with $\tilde{\mathbf{f}}_{\mathbf{u}}$ (c) Assimilation with $\mathbf{R}_{\gamma\delta}$

(d) Assimilation with β (e) Assimilation with $\tilde{f}_{\tilde{\nu}}$ (f) Assimilation with $\tilde{g}_{\tilde{\nu}}$

FIG. 18: f_x for RANS-SA, $\tilde{\mathbf{f}}_{\mathbf{u}}$, $\mathbf{R}_{\gamma\delta}$, β, $\tilde{f}_{\tilde{\nu}}$ and $\tilde{g}_{\tilde{\nu}}$

VI. DISCUSSION DIRECTED TO MACHINE-LEARNING APPLICATIONS

Although our study aims to address a general framework concerning data-assimilation approaches, one of the main motivations of this study concerns the augmentation of turbulence models based on field-inversion techniques [20]. Therefore, pros and cons are highlighted in this section considering that researchers and engineers may want to further apply machine-learning to enhance turbulence models.

The correction through $\tilde{\mathbf{f}}_{\mathbf{u}}$ and $\mathbf{R}_{\gamma\delta}$ are the ones that best recovered the reference field. Both corrections are not restricted to the Boussinesq hypotheses nor eddy-viscosity models and they excelled even for the highly unstable mean flow over the square cylinder. $\mathbf{R}_{\gamma\delta}$ has the advantage of directly providing the anistropic component of the

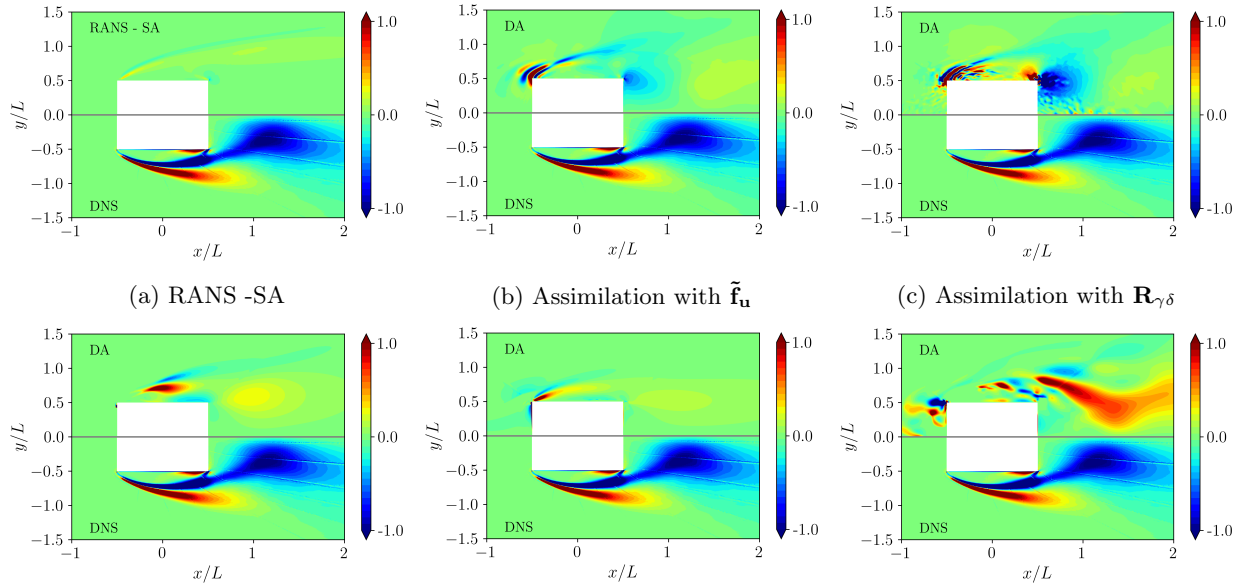

(a) RANS -SA (b) Assimilation with $\tilde{\mathbf{f}}_{\mathbf{u}}$ (c) Assimilation with $\mathbf{R}_{\gamma\delta}$

(d) Assimilation with β (e) Assimilation with $\tilde{f}_{\tilde{\nu}}$ (f) Assimilation with $\tilde{g}_{\tilde{\nu}}$

FIG. 19: f_y for RANS-SA, $\tilde{\mathbf{f}}_{\mathbf{u}}$, $\mathbf{R}_{\gamma\delta}$, β, $\tilde{f}_{\tilde{\nu}}$ and $\tilde{g}_{\tilde{\nu}}$

Reynolds stress tensor but with the downside of additional derivatives computations. For machine-learning purposes, $\tilde{\mathbf{f}}_{\mathbf{u}}$ and $\mathbf{R}_{\gamma\delta}$ demand more computational resource due to their vectorial/tensor form and guaranteeing the rotational invariance can be non trivial (especially in 3D) [26, 50]. Besides, they are dimensional quantities, which may pose an additional difficulty to the generalization process.

In spite of being constrained to the Boussinesq hypothesis, the $\tilde{\mathbf{g}}_{\tilde{\nu}}$ assimilation had results comparable to the ones of $\tilde{\mathbf{f}}_{\mathbf{u}}$ and $\mathbf{R}_{\gamma\delta}$ for all three cases. The results for our flow cases indicated the possibility of correcting the velocity field by means of an eddy-viscosity model even in the presence of great separation. Moreover, the $\tilde{\mathbf{g}}_{\tilde{\nu}}$ is a scalar field, consequently, it would require less computational cost to be modelled by machine-learning techniques.

The β parameter was one of the first quantities to be studied in the Field-Inversion/Machine-Learning framework [11, 20]. Differently from the other source terms in the SA equation, it aims at fixing the production of the turbulence viscosity. This parameter is very interesting from a FIML perspective because it is a non-dimensional scalar quantity. This can facilitate the learning process of a neural network algorithm (differently from vectors and tensors). One drawback of the β type correction is its limitation to assimilate the velocity field compared to the other control terms. The same drawback can be addressed to $\tilde{f}_{\tilde{\nu}}$.

The multiplicative term ξ in the eddy-viscosity was able to partially correct the channel flow but performed poorly for the periodic-hill and square-cylinder flow. The advantages of this method are that it can provide corrections that are independent from the eddy-viscosity transport equation, and the correction is a scalar and dimensionless quantity. We showed that this approach lacks accuracy and robustness at least for the types of flows studied herein. Nevertheless, this eddy-viscosity correction can be easily estimated based on other assimilation procedures and generalized using ML to improve a RANS model as done in [41]. Table III summarizes what was discussed in this section.

VII. CONCLUSIONS

In this work, we studied different correction approaches in data-assimilation procedures in order to quantify their performance in recovering the reference solution taking into consideration the same mesh, numerical methods and cost functional. The assimilations were made by including correction terms in the averaged momentum equations, the Spalart-Allmaras model and the eddy-viscosity field. Tests were performed in three different cases: a limited-separated flow in a convergent-divergent channel, the flow over periodic hills and a strongly separated flow over a square cylinder. The first approach (i.e., correction through forcing terms in the averaged momentum equations) demonstrated better performance overall, justified by the fact that the data assimilation associated with these quantities is not restricted to the Boussinesq hypothesis. The second approach (correction through terms in the Spalart-Allmaras model) recovered in general the mean field for the two first cases, however the correction of the square cylinder flow was partial for β

TABLE III: Summary table about the performance of each assimilation for the presented cases with pros and cons of each control term chosen. CDC: Convergent-divergent channel, PH: Periodic hills, SC: Square cylinder. Double check, single check, and x-mark indicates the correction performance, from best to worst; x-mark being failure

Control term	CDC	PH	SC	Pros for ML applications	Cons for ML applications
$\tilde{\mathbf{f}}_{\mathbf{u}}$	✓✓	✓✓	✓✓	Excellent precision, robustness and not constrained to the Boussinesq hypotheses	Dimensional quantity, additional complexity in 3D, source term in the momentum equation
$\mathbf{R}_{\gamma\delta}$	✓✓	✓✓	✓✓	Excellent precision, robustness and not constrained to the Boussinesq hypotheses	Dimensional quantity, additional complexity in 3D
β	✓	✓	✓	Naturally dimensionless, good performance, scalar field	Constrained to the Boussinesq hypotheses
$\tilde{f}_{\tilde{\nu}}$	✓✓	✓✓	✓	Good performance, scalar field	Constrained to the Boussinesq hypotheses and not naturally dimensionless
$\tilde{g}_{\tilde{\nu}}$	✓✓	✓✓	✓✓	Excellent precision, scalar field	Constrained to the Boussinesq hypotheses and not naturally dimensionless
ξ	✓	✓	✗	Naturally dimensionless, scalar field	Constrained to the Boussinesq hypotheses, poor performance and robustness

and $\tilde{f}_{\tilde{\nu_t}}$. Interestingly, the $\tilde{g}_{\tilde{\nu_t}}$ control term showed good performance for all three cases, even the most challenging one, the square cylinder. Both source terms $\tilde{f}_{\tilde{\nu}}$ and $\tilde{g}_{\tilde{\nu}}$ fix the balance of production, destruction and cross-diffusion in the SA equation, but the latter term is conditioned by the turbulence variable in order to reject unphysical corrections at locations where turbulence is weak. We showed that this constraint helps the optimization procedure and improves the assimilation results. The study showed that the performance of the second approach can be highly dependent on the control term chosen in the Spalart-Allmaras model (β, $\tilde{f}_{\tilde{\nu_t}}$ and $\tilde{g}_{\tilde{\nu_t}}$). The third approach (correction of the eddy-viscosity field) was not as satisfactory as the others, even though it improved the final velocity field for the first two cases. The optimization of the inverse problem for that approach was particularly troublesome for the flow over the square cylinder. We showed that trying to fix the turbulence-eddy viscosity based on the ξ-correction gives less accurate results than the other Boussinesq-like corrections and that placing the correction terms directly on the SA model improves numerical robustness regardless of the test case. Concerning the reconstruction of the skin-friction profile, the best assimilation parameters were clearly $\tilde{\mathbf{f}}_{\mathbf{u}}$, $\mathbf{R}_{\gamma\delta}$ and $\tilde{g}_{\tilde{\nu_t}}$. One important finding of this study is that it is possible to accurately reconstruct the mean field, despite the usage of the Boussinesq hypothesis and misprediction of the Reynolds stresses. As a matter of fact, the $\tilde{g}_{\tilde{\nu_t}}$-correction not only successfully improved the velocity field, but it also predicted a realistic Reynolds stress and force vector in a large part of the domain. It is worthy noting that this study treated data assimilation using only dense velocity field measurements. Therefore, further analysis is needed when considering sparse reference data.

Appendix A: Derivation of adjoint equations

The adjoint set of equations to be solved are computed from the Frchet derivative of the Lagrangian, from equation 10, with respect to the state vector $\tilde{\mathbf{q}}$. It is written as:

$$\begin{aligned}
\frac{\partial L}{\partial \tilde{\mathbf{q}}}\delta\tilde{\mathbf{q}} = \lim_{\varepsilon\to 0}\frac{1}{\varepsilon}\Big\{ & J(\tilde{\mathbf{u}}+\varepsilon\delta\tilde{\mathbf{u}}) + \langle \tilde{\mathbf{u}}^\dagger, (\tilde{\mathbf{u}}+\varepsilon\delta\tilde{\mathbf{u}})\cdot\nabla(\tilde{\mathbf{u}}+\varepsilon\delta\tilde{\mathbf{u}}) + \nabla(p+\varepsilon\delta p) \\
& -\nabla\cdot\left[\left(\nu+(1+\xi)\left[\nu_t(\tilde{\nu}+\varepsilon\delta\tilde{\nu})\right]\right)\nabla_s(\tilde{\mathbf{u}}+\varepsilon\delta\tilde{\mathbf{u}}) + \mathbf{R}_{\gamma\delta}\right] - \tilde{\mathbf{f}}_{\mathbf{u}}\rangle_\Omega + \langle \tilde{p}^\dagger, \nabla\cdot(\tilde{\mathbf{u}}+\varepsilon\delta\tilde{\mathbf{u}})\rangle_\Omega \\
& +\langle \tilde{\nu}^\dagger, (\tilde{\mathbf{u}}+\varepsilon\delta\tilde{\mathbf{u}})\cdot\nabla(\tilde{\nu}+\varepsilon\delta\tilde{\nu}) - \nabla\cdot\left[\left[\eta(\tilde{\nu}+\varepsilon\delta\tilde{\nu})\right]\nabla(\tilde{\nu}+\varepsilon\delta\tilde{\nu})\right] - s(\tilde{\nu}+\varepsilon\delta\tilde{\nu}, \nabla(\tilde{\nu}+\varepsilon\delta\tilde{\nu}), \nabla(\tilde{\mathbf{u}}+\varepsilon\delta\tilde{\mathbf{u}})) - \tilde{f}_{\tilde{\nu}} \\
& -\tilde{g}_{\tilde{\nu}}(\tilde{\nu}+\varepsilon\delta\tilde{\nu})\rangle_\Omega - J(\tilde{\mathbf{u}}) - \langle \tilde{\mathbf{u}}^\dagger, \tilde{\mathbf{u}}\cdot\nabla\tilde{\mathbf{u}} + \nabla p - \nabla\cdot\left[\left(\nu+(1+\xi)\,\nu_t(\tilde{\nu})\right)\nabla_s\tilde{\mathbf{u}} + \mathbf{R}_{\gamma\delta}\right] - \tilde{\mathbf{f}}_{\mathbf{u}}\rangle_\Omega - \langle \tilde{p}^\dagger, \nabla\cdot\tilde{\mathbf{u}}\rangle_\Omega \\
& -\langle \tilde{\nu}^\dagger, \tilde{\mathbf{u}}\cdot\nabla\tilde{\nu} - \nabla\cdot(\eta(\tilde{\nu})\nabla\tilde{\nu}) - s(\tilde{\nu}, \nabla\tilde{\nu}, \nabla\tilde{\mathbf{u}}) - \tilde{f}_{\tilde{\nu}} - \tilde{g}_{\tilde{\nu}}\tilde{\nu}\rangle_\Omega\Big\}
\end{aligned} \tag{A1}$$

The source term of the Spalart-Allmaras model can be expanded as:

$$\begin{aligned}
& s(\tilde{\nu}+\varepsilon\delta\tilde{\nu}, \nabla(\tilde{\nu}+\varepsilon\delta\tilde{\nu}), \nabla(\tilde{\mathbf{u}}+\varepsilon\delta\tilde{\mathbf{u}})) \approx \\
& s(\tilde{\nu}, \nabla(\tilde{\nu}), \nabla(\tilde{\mathbf{u}})) + \varepsilon\delta\tilde{\nu}\frac{\partial s}{\partial\tilde{\nu}} + \varepsilon\nabla(\delta\tilde{\nu})\cdot\frac{\partial s}{\partial(\nabla(\tilde{\nu}))} + \varepsilon\nabla(\delta\tilde{\mathbf{u}}) : \frac{\partial s}{\partial(\nabla(\tilde{\mathbf{u}}))} \\
& = s(\tilde{\nu}, \nabla(\tilde{\nu}), \nabla(\tilde{\mathbf{u}})) + \varepsilon\delta\tilde{\nu}\partial_{\tilde{\nu}}s + \varepsilon\nabla(\delta\tilde{\nu})\cdot\partial_{\nabla(\tilde{\nu})}s + \varepsilon\nabla(\delta\tilde{\mathbf{u}}) : \partial_{\nabla(\tilde{\mathbf{u}})}s
\end{aligned} \tag{A2}$$

The terms $J(\tilde{\mathbf{u}}+\varepsilon\delta\tilde{\mathbf{u}})$, $\nu_t(\tilde{\nu}+\varepsilon\delta\tilde{\nu})$ and $\eta(\tilde{\nu}+\varepsilon\delta\tilde{\nu})$ can also be expanded. If one substitutes the above expansions in equation A1, considering only the first order terms, the equation becomes:

$$\begin{aligned}
\frac{\partial L}{\partial \tilde{\mathbf{q}}}\delta\tilde{\mathbf{q}} = \lim_{\varepsilon\to 0}\frac{1}{\varepsilon}\Bigg\{ & \varepsilon\delta\tilde{\mathbf{u}}\frac{\partial J}{\partial\tilde{\mathbf{u}}} + \langle \tilde{\mathbf{u}}^\dagger, \varepsilon\delta\tilde{\mathbf{u}}\cdot\nabla\tilde{\mathbf{u}} + \tilde{\mathbf{u}}\cdot\nabla(\varepsilon\delta\tilde{\mathbf{u}}) + \nabla(\varepsilon\delta p) \\
& -\nabla\cdot\left(\left(\nu+(1+\xi)\,\nu_t\right)\nabla_s(\varepsilon\delta\tilde{\mathbf{u}})\right) - \nabla\cdot\left(\left((1+\xi)\,\varepsilon\delta\tilde{\nu}\frac{\partial\nu_t}{\partial\tilde{\nu}}\right)\nabla_s\tilde{\mathbf{u}}\right)\rangle_\Omega + \langle \tilde{p}^\dagger, \nabla\cdot(\varepsilon\delta\tilde{\mathbf{u}})\rangle_\Omega \\
& +\langle \tilde{\nu}^\dagger, \tilde{\mathbf{u}}\cdot\nabla(\varepsilon\delta\tilde{\nu}) + (\varepsilon\delta\tilde{\mathbf{u}})\cdot\nabla\tilde{\nu} - \nabla\cdot(\eta\nabla(\varepsilon\delta\tilde{\nu})) - \nabla\cdot(\varepsilon\delta\tilde{\nu}\frac{\partial\eta}{\partial\tilde{\nu}}\nabla\tilde{\nu}) \\
& -\varepsilon\delta\tilde{\nu}\partial_{\tilde{\nu}}s - \varepsilon\nabla(\delta\tilde{\nu})\cdot\partial_{\nabla\tilde{\nu}}s - \varepsilon\nabla\delta\tilde{\mathbf{u}} : \partial_{\nabla(\tilde{\mathbf{u}})}s - \tilde{g}_{\tilde{\nu}}\varepsilon\delta\tilde{\nu}\rangle_\Omega\Bigg\}
\end{aligned} \tag{A3}$$

Or

$$\begin{aligned}
\frac{\partial L}{\partial \tilde{\mathbf{q}}}\delta\tilde{\mathbf{q}} = & \delta\tilde{\mathbf{u}}\frac{\partial J}{\partial\tilde{\mathbf{u}}} + \langle \tilde{\mathbf{u}}^\dagger, \delta\tilde{\mathbf{u}}\cdot\nabla\tilde{\mathbf{u}} + \tilde{\mathbf{u}}\cdot\nabla\delta\tilde{\mathbf{u}} + \nabla\delta p \\
& -\nabla\cdot\left(\left(\nu+(1+\xi)\,\nu_t\right)\nabla_s\delta\tilde{\mathbf{u}}\right) - \nabla\cdot\left(\left((1+\xi)\,\delta\tilde{\nu}\frac{\partial\nu_t}{\partial\tilde{\nu}}\right)\nabla_s\tilde{\mathbf{u}}\right)\rangle_\Omega + \langle \tilde{p}^\dagger, \nabla\cdot\delta\tilde{\mathbf{u}}\rangle_\Omega \\
& +\langle \tilde{\nu}^\dagger, \tilde{\mathbf{u}}\cdot\nabla\delta\tilde{\nu} + \delta\tilde{\mathbf{u}}\cdot\nabla\tilde{\nu} - \nabla\cdot(\eta\nabla\delta\tilde{\nu}) - \nabla\cdot(\delta\tilde{\nu}\frac{\partial\eta}{\partial\tilde{\nu}}\nabla\tilde{\nu}) \\
& -\delta\tilde{\nu}\partial_{\tilde{\nu}}s - \nabla\delta\tilde{\nu}\cdot\partial_{\nabla\tilde{\nu}}s - \nabla\delta\tilde{\mathbf{u}} : \partial_{\nabla(\tilde{\mathbf{u}})}s - \tilde{g}_{\tilde{\nu}}\delta\tilde{\nu}\rangle_\Omega
\end{aligned} \tag{A4}$$

Equation A4 is set to zero for any variation of the state variables assumed. Integration by parts is used in order to put the variational terms out of the differential operators. Each term from the RHS, starting from the second one, is rewritten and integrated by parts. They are numbered from I to $XIII$ and are developed as follows.

Terms I and II:

$$\begin{aligned}
& \langle \tilde{\mathbf{u}}^\dagger, \tilde{\mathbf{u}}\cdot\nabla\delta\tilde{\mathbf{u}}\rangle_\Omega + \langle \tilde{\mathbf{u}}^\dagger, \delta\tilde{\mathbf{u}}\cdot\nabla\tilde{\mathbf{u}}\rangle_\Omega = \\
& -\langle \delta\tilde{\mathbf{u}}, (\tilde{\mathbf{u}}\cdot\nabla)\tilde{\mathbf{u}}^\dagger\rangle_\Omega + \langle \delta\tilde{\mathbf{u}}, \tilde{\mathbf{u}}^\dagger\nabla\tilde{\mathbf{u}}^T\rangle_\Omega + \langle \delta\tilde{\mathbf{u}}, \tilde{\mathbf{u}}^\dagger(\tilde{\mathbf{u}}\cdot\mathbf{n})\rangle_\delta
\end{aligned} \tag{A5}$$

Term III:

$$\langle \tilde{\mathbf{u}}^\dagger, \nabla\delta p\rangle_\Omega = -\langle \nabla\cdot\tilde{\mathbf{u}}^\dagger, \delta p\rangle_\Omega + \langle \tilde{\mathbf{u}}^\dagger\cdot\mathbf{n}, \delta p\rangle_\delta \tag{A6}$$

Term IV:

$$\begin{aligned}\langle\tilde{\mathbf{u}}^\dagger, -\nabla\cdot\left(\left(\nu+(1+\xi)\,\nu_t\right)\nabla_s\delta\tilde{\mathbf{u}}\right)\rangle_\Omega = \\ -\langle\delta\tilde{\mathbf{u}},\nabla\cdot(\nu+(1+\xi)\nu_t)\nabla_s\tilde{\mathbf{u}}^\dagger\rangle_\Omega + \langle\delta\tilde{\mathbf{u}},(\nu+(1+\xi)\nu_t)(\nabla_s\tilde{\mathbf{u}}^\dagger)\mathbf{n}\rangle_\delta \\ -\langle\tilde{\mathbf{u}}^\dagger,(\nu+(1+\xi)\nu_t)(\nabla_s\delta\tilde{\mathbf{u}})\mathbf{n}\rangle_\delta\end{aligned} \tag{A7}$$

Term V:

$$\begin{aligned}\langle\tilde{\mathbf{u}}^\dagger, -\nabla\cdot\left(\left((1+\xi)\,\delta\tilde{\nu}\frac{\partial\nu_t}{\partial\tilde{\nu}}\right)\nabla_s\tilde{\mathbf{u}}\right)\rangle_\Omega = \\ \langle(1+\xi)\,\delta\tilde{\nu}\frac{\partial\nu_t}{\partial\tilde{\nu}},\nabla\tilde{\mathbf{u}}^\dagger:\nabla_s\tilde{\mathbf{u}}\rangle_\Omega - \langle\tilde{\mathbf{u}}^\dagger,\left((1+\xi)\,\delta\tilde{\nu}\frac{\partial\nu_t}{\partial\tilde{\nu}}\right)\nabla_s\tilde{\mathbf{u}}\cdot\mathbf{n}\rangle_\delta\end{aligned} \tag{A8}$$

Term VI:

$$\langle\tilde{p}^\dagger,\nabla\cdot\delta\tilde{\mathbf{u}}\rangle_\Omega = -\langle\nabla\tilde{p}^\dagger,\delta\tilde{\mathbf{u}}\rangle_\Omega + \langle\tilde{p}^\dagger\mathbf{n},\delta\tilde{\mathbf{u}}\rangle_\delta \tag{A9}$$

Terms VII and $VIII$:

$$\langle\tilde{\nu}^\dagger,\tilde{\mathbf{u}}\cdot\nabla\delta\tilde{\nu}+\delta\tilde{\mathbf{u}}\cdot\nabla\tilde{\nu}\rangle_\Omega = -\langle\delta\tilde{\nu},\nabla\tilde{\nu}^\dagger\cdot\tilde{\mathbf{u}}\rangle_\Omega + \langle\delta\tilde{\mathbf{u}},\tilde{\nu}^\dagger\nabla\tilde{\nu}\rangle_\Omega + \langle\delta\tilde{\nu},\tilde{\nu}^\dagger\tilde{\mathbf{u}}\cdot\mathbf{n}\rangle_\delta \tag{A10}$$

Term IX:

$$\langle\tilde{\nu}^\dagger,-\nabla\cdot(\eta\nabla\delta\tilde{\nu})\rangle_\Omega = -\langle\delta\tilde{\nu},\nabla\cdot(\nabla\tilde{\nu}^\dagger\eta)\rangle_\Omega + \langle\delta\tilde{\nu},\eta\nabla\tilde{\nu}^\dagger\cdot\mathbf{n}\rangle_\delta - \langle\tilde{\nu}\eta,\nabla\delta\tilde{\nu}\cdot\mathbf{n}\rangle_\delta \tag{A11}$$

Term X:

$$\langle\tilde{\nu}^\dagger,-\nabla\cdot(\delta\tilde{\nu}\frac{\partial\eta}{\partial\tilde{\nu}}\nabla\tilde{\nu})\rangle_\Omega = \langle\delta\tilde{\nu},\partial_{\tilde{\nu}}\eta\nabla\tilde{\nu}^\dagger\cdot\nabla\tilde{\nu}\rangle_\Omega - \langle\delta\tilde{\nu},\partial_{\tilde{\nu}}\eta\tilde{\nu}^\dagger\nabla\tilde{\nu}\cdot\mathbf{n}\rangle_\delta \tag{A12}$$

Term XI:

$$\langle\tilde{\nu}^\dagger,-\delta\tilde{\nu}\partial_{\tilde{\nu}}s\rangle_\Omega = -\langle\delta\tilde{\nu},\tilde{\nu}^\dagger\partial_{\tilde{\nu}}s\rangle_\Omega \tag{A13}$$

Term XII:

$$\langle\tilde{\nu}^\dagger,-\nabla\delta\tilde{\nu}\cdot\partial_{\nabla(\tilde{\nu})}s\rangle_\Omega = \langle\delta\tilde{\nu},\nabla\cdot(\tilde{\nu}^\dagger\partial_{\nabla\tilde{\nu}}s)\rangle_\Omega - \langle\delta\tilde{\nu},\tilde{\nu}^\dagger\partial_{\nabla\tilde{\nu}}s\cdot\mathbf{n}\rangle_\delta \tag{A14}$$

Term $XIII$:

$$\langle\tilde{\nu}^\dagger,-\nabla\delta\tilde{\mathbf{u}}:\partial_{\nabla(\tilde{\mathbf{u}})}s\rangle_\Omega = \langle\delta\tilde{\mathbf{u}},\nabla\cdot\left(\tilde{\nu}^\dagger\partial_{\nabla(\tilde{\mathbf{u}})}s\right)\rangle_\Omega - \langle\delta\tilde{\mathbf{u}},\tilde{\nu}^\dagger\partial_{\nabla\tilde{\mathbf{u}}}s\cdot\mathbf{n}\rangle_\delta \tag{A15}$$

The terms containing integrals over the domain originate the adjoint equations while the terms over the boundaries originate the adjoint boundary conditions. If the terms with $\delta\tilde{\mathbf{u}}$ are grouped and set to zero for any $\delta\tilde{\mathbf{u}}$, one has the adjoint equation analogous to the momentum equation. For the term with $\delta\tilde{p}$, one has an equation similar to the incompressibility. Finally, the terms with $\delta\tilde{\nu}$ gives the adjoint equation for the adjoint eddy-viscosity. In summary:

$$\begin{aligned}\frac{\partial L}{\partial\tilde{\mathbf{q}}}\delta\tilde{\mathbf{q}} = \delta\tilde{\mathbf{u}}\frac{\partial J}{\partial\tilde{\mathbf{u}}} + -\langle\delta\tilde{\mathbf{u}},(\tilde{\mathbf{u}}\cdot\nabla)\tilde{\mathbf{u}}^\dagger\rangle_\Omega + \langle\delta\tilde{\mathbf{u}},\tilde{\mathbf{u}}^\dagger\nabla\tilde{\mathbf{u}}^T\rangle_\Omega - \langle\nabla\cdot\tilde{\mathbf{u}}^\dagger,\delta p\rangle_\Omega \\ -\langle\delta\tilde{\mathbf{u}},\nabla\cdot(\nu+(1+\beta)\nu_T)\nabla_s\tilde{\mathbf{u}}^\dagger\rangle_\Omega + \langle(1+\xi)\,\delta\tilde{\nu}\frac{\partial\nu_t}{\partial\tilde{\nu}},\nabla\tilde{\mathbf{u}}^\dagger:\nabla_s\tilde{\mathbf{u}}\rangle_\Omega - \langle\nabla\tilde{p}^\dagger,\delta\tilde{\mathbf{u}}\rangle_\Omega \\ -\langle\delta\tilde{\nu},\nabla\tilde{\nu}^\dagger\cdot\tilde{\mathbf{u}}\rangle_\Omega + \langle\delta\tilde{\mathbf{u}},\tilde{\nu}^\dagger\nabla\tilde{\nu}\rangle_\Omega - \langle\delta\tilde{\nu},\nabla\cdot(\nabla\tilde{\nu}^\dagger\eta)\rangle_\Omega + \langle\delta\tilde{\nu},\partial_{\tilde{\nu}}\eta\nabla\tilde{\nu}^\dagger\cdot\nabla\tilde{\nu}\rangle_\Omega \\ -\langle\delta\tilde{\nu},\tilde{\nu}^\dagger\partial_{\tilde{\nu}}s\rangle_\Omega + \langle\delta\tilde{\nu},\nabla\cdot(\tilde{\nu}^\dagger\partial_{\nabla\tilde{\nu}}s)\rangle_\Omega + \langle\delta\tilde{\mathbf{u}},\nabla\cdot\left(\tilde{\nu}^\dagger\partial_{\nabla(\tilde{\mathbf{u}})}s\right)\rangle_\Omega - \langle\delta\tilde{\nu},\tilde{\nu}^\dagger\tilde{g}_{\tilde{\nu}}\rangle_\Omega + \text{boundary integrals}\end{aligned} \tag{A16}$$

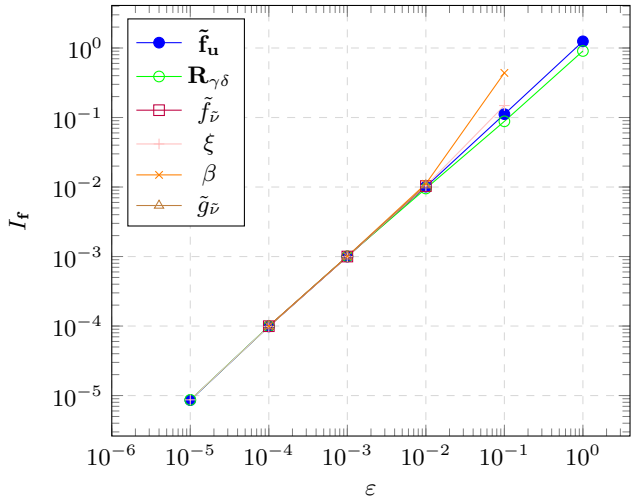

FIG. 20: Gradient test

Which gives the adjoint equations:

$$\begin{gathered}
\nabla \cdot \tilde{\mathbf{u}}^\dagger = 0, \\
\tilde{\mathbf{u}}^\dagger \cdot (\nabla \tilde{\mathbf{u}})^T - \tilde{\mathbf{u}} \cdot \nabla \tilde{\mathbf{u}}^\dagger - \nabla \cdot \left[(\nu + (1+\xi)\nu_t) \nabla_s \tilde{\mathbf{u}}^\dagger \right] - \nabla \tilde{p}^\dagger + \tilde{\nu}^\dagger \nabla \tilde{\nu} + \nabla \cdot \left(\tilde{\nu}^\dagger \partial_{\nabla \tilde{u}} s \right) \\
= -(\tilde{\mathbf{u}} - \overline{\mathbf{u}}), \\
-\tilde{\mathbf{u}} \cdot \nabla \tilde{\nu}^\dagger - \nabla \cdot \left(\eta \nabla \tilde{\nu}^\dagger \right) + (\partial_{\tilde{\nu}} \eta) \nabla \tilde{\nu}^\dagger \cdot \nabla \tilde{\nu} + (1+\xi) (\partial_{\tilde{\nu}} \nu_t) \nabla \tilde{\mathbf{u}}^\dagger : \nabla_s \tilde{\mathbf{u}} - (\partial_{\tilde{\nu}} s) \tilde{\nu}^\dagger + \nabla \cdot \left(\tilde{\nu}^\dagger \partial_{\nabla \tilde{\nu}} s \right) - \tilde{\nu}^\dagger \tilde{g}_{\tilde{\nu}} = 0.
\end{gathered} \tag{A17}$$

Appendix B: Gradient test

Given the cost functional $J = J(\mathbf{f})$ and a small variation of the control vector $\mathbf{f}$, written as $\varepsilon\delta\mathbf{f}$, the cost functional can be expanded as

$$J(\mathbf{f} + \varepsilon\delta\mathbf{f}) = J(\mathbf{f}) + \varepsilon \langle \nabla_\mathbf{f} J, \delta\mathbf{f} \rangle + O\left(\varepsilon^2\right) \tag{B1}$$

with ε a small parameter. Honnorat[51] details a procedure to verify if the gradient computed from the adjoint approach matches to the true gradient. In order to do the test, the gradient is computed by means of a forward finite differences and the ratio defined $I_\mathbf{f}$ is defined as

$$I_\mathbf{f} = \frac{J(\mathbf{f} + \varepsilon\delta\mathbf{f}) - J(\mathbf{f})}{\langle \nabla_\mathbf{f} J, \delta\mathbf{f} \rangle} \tag{B2}$$

and the property $\lim_{\mathbf{f}\to 0} I_\mathbf{f} = 1$ should be verified. The value of $I_\mathbf{f}$ is plotted against ε in Figure B for four representative cases. As the finite differences used was of first order, the overall linear behavior is expected.

In order to verify if a local minimum is being approached, the relative L_2 norm of each gradient is plotted in Figure 21. In the end of the assimilation procedures, most of the gradients decreased of three or four orders of magnitude, except the gradient with respect to ξ, which after the first iterations remains on a high plateau. This might be due to precision issues due to the fact that the gradient with respect ξ, shown in eq. (12), involves many (two) gradients.

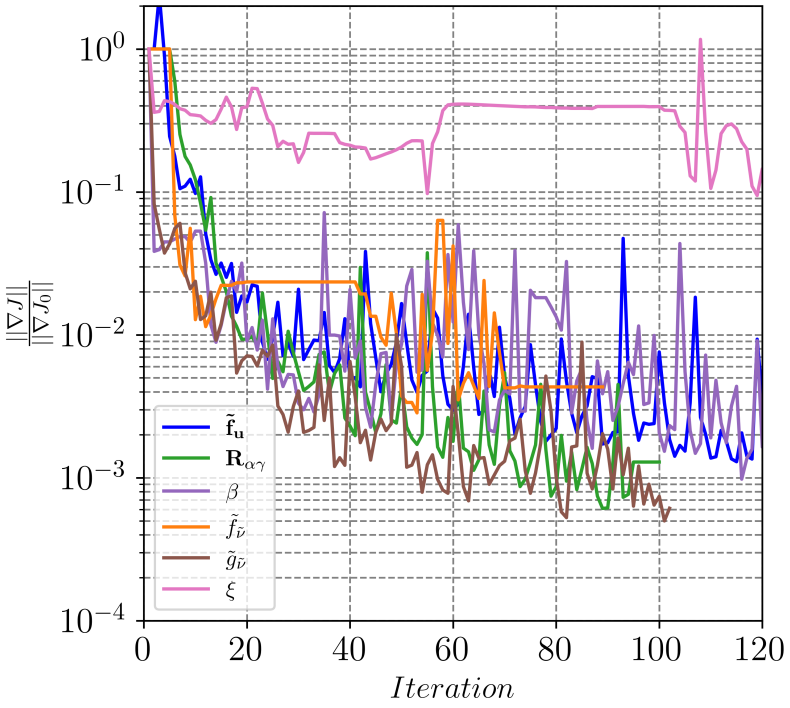

FIG. 21: $\frac{\|\nabla J\|}{\|\nabla J_0\|}$ during data-assimilation iterations.

Acknowledgments

This work was supported by ONERA under projects HORUS and MODDA.

[1] P. Spalart and S. Allmaras, in *30th Aerospace Sciences Meeting and Exhibit* (1992), URL https://doi.org/10.2514/6.1992-439.

[2] B. Launder and D. Spalding, Computer Methods in Applied Mechanics and Engineering **3**, 269 (1974), ISSN 0045-7825, URL https://www.sciencedirect.com/science/article/pii/0045782574900292.

[3] D. C. Wilcox, AIAA J. **46**, 2823 (2008), URL https://doi.org/10.2514/1.36541.

[4] H. Xiao and P. Cinnella, Progress in Aerospace Sciences **108**, 1 (2019), ISSN 0376-0421, URL https://doi.org/10.1016/j.paerosci.2018.10.001.

[5] Z. Li, H. Zhang, S. C. C. Bailey, J. B. Hoagg, and A. Martin, J. Comput. Phys. **345**, 111 (2017), URL https://doi.org/10.1016/j.jcp.2017.05.009.

[6] D. P. G. Foures, N. Dovetta, D. Sipp, and P. J. Schmid, J. Fluid Mech. **759**, 404431 (2014), URL https://doi.org/10.1017/jfm.2014.566.

[7] L. Franceschini, D. Sipp, and O. Marquet, Phys. Rev. Fluids **5**, 094603 (2020), URL https://link.aps.org/doi/10.1103/PhysRevFluids.5.094603.

[8] S. Li, C. He, and Y. Liu, Phys. Fluids **34**, 015101 (2022), URL https://doi.org/10.1063/5.0076754.

[9] A. P. Singh, K. Duraisamy, and Z. J. Zhang, in *55th AIAA Aerospace Sciences Meeting* (2017), URL https://doi.org/10.2514/6.2017-0993.

[10] G. Suarez, B. Y. Zhou, E. Oezkaya, R. Pochampalli, and N. R. Gauger, in *AIAA AVIATION 2021 FORUM* (2021), URL https://doi.org/10.2514/6.2021-3088.

[11] A. P. Singh, S. Medida, and K. Duraisamy, AIAA J. **55**, 2215 (2017), URL https://doi.org/10.2514/1.J055595.

[12] M. B. Ali, G. Tissot, S. Aguinaga, D. Heitz, and E. Mémin, Journal of Wind Engineering and Industrial Aerodynamics **231**, 105204 (2022), URL https://doi.org/10.1016/j.jweia.2022.105204.

[13] J.-X. Wang, J.-L. Wu, and H. Xiao, Phys. Rev. Fluids **2**, 034603 (2017), URL https://doi.org/10.1103/PhysRevFluids.2.034603.

[14] J.-L. Wu, H. Xiao, and E. Paterson, Phys. Rev. Fluids **3**, 074602 (2018), URL https://doi.org/10.1103/PhysRevFluids.3.074602.

[15] J. Ling, A. Kurzawski, and J. Templeton, J. Fluid Mech. **807**, 155166 (2016), URL https://doi.org/10.1017/jfm.2016.615.

[16] J. Wu, H. Xiao, R. Sun, and Q. Wang, Journal of Fluid Mechanics **869**, 553 (2019), URL https://doi.org/10.1017/jfm.2019.205.

[17] B. P. Brener, M. A. Cruz, R. L. Thompson, and R. P. Anjos, Journal of Fluid Mechanics **915**, A110 (2021), URL https://doi.org/10.1017/jfm.2021.148.

[18] M. A. Cruz, R. L. Thompson, L. E. Sampaio, and R. D. Bacchi, Computers & Fluids **192**, 104258 (2019), URL https://doi.org/10.1016/j.compfluid.2019.104258.

[19] S. Berrone and D. Oberto, Physics of Fluids **34** (2022), URL https://doi.org/10.1063/5.0104605.

[20] E. J. Parish and K. Duraisamy, J. Comput. Phys. **305**, 758 (2016), ISSN 0021-9991, URL https://doi.org/10.1016/j.jcp.2015.11.012.

[21] K. Duraisamy, G. Iaccarino, and H. Xiao, Annual Review of Fluid Mechanics **51**, 357 (2019), URL https://doi.org/10.1146/annurev-fluid-010518-040547.

[22] K. Duraisamy, Phys. Rev. Fluids **6**, 050504 (2021), URL https://doi.org/10.1103/PhysRevFluids.6.050504.

[23] F. Khler, J. Munz, and M. Schfer, in *AIAA Scitech 2020 Forum* (2020), URL https://doi.org/10.2514/6.2020-1586.

[24] A. Ferrero, A. Iollo, and F. Larocca, Comput. and Fluids **201**, 104474 (2020), ISSN 0045-7930, URL https://doi.org/10.1016/j.compfluid.2020.104474.

[25] C. L. Rumsey, G. N. Coleman, and L. Wang, in *AIAA SCITECH 2022 Forum* (2022), URL https://doi.org/10.2514/6.2022-0937.

[26] P. S. Volpiani, M. Meyer, L. Franceschini, J. Dandois, F. Renac, E. Martin, O. Marquet, and D. Sipp, Phys. Rev. Fluids **6**, 064607 (2021), URL https://doi.org/10.1103/PhysRevFluids.6.064607.

[27] A. Crivellini, V. DAlessandro, and F. Bassi, Journal of Computational Physics **241**, 388 (2013), URL https://doi.org/10.1016/j.jcp.2012.12.038.

[28] A. P. Singh and K. Duraisamy, Phys. Fluids **28**, 045110 (2016), URL https://doi.org/10.1063/1.4947045.

[29] U. Schumann, The Physics of Fluids **20**, 721 (1977), URL https://doi.org/10.1063/1.861942.

[30] F. Hecht, J. Numer. Math. **20**, 251 (2012), ISSN 1570-2820, URL https://freefem.org/.

[31] Y. Bao, D. Zhou, C. Huang, Q. Wu, and X. qiao Chen, Computers & Structures **89**, 325 (2011), ISSN 0045-7949, URL https://doi.org/10.1016/j.compstruc.2010.10.019.

[32] A. N. Brooks and T. J. Hughes, Computer Methods in Applied Mechanics and Engineering **32**, 199 (1982), ISSN 0045-7825, URL https://doi.org/10.1016/0045-7825(82)90071-8.

[33] P. Amestoy, I. S. Duff, J. Koster, and J.-Y. L'Excellent, SIAM Journal on Matrix Analysis and Applications **23**, 15 (2001), URL https://doi.org/10.1137/S0895479899358194.

[34] P. Amestoy, A. Buttari, J.-Y. L'Excellent, and T. Mary, ACM Transactions on Mathematical Software **45**, 2:1 (2019), URL https://doi.org/10.1145/3242094.

[35] A. Bernard, J. M. Foucaut, P. Dupont, and M. Stanislas, AIAA J. **41**, 248 (2003), URL https://doi.org/10.2514/2.1937.

[36] M. Marquillie, J.-P. Laval, and R. Dolganov, J. Turb. **9**, N1 (2008), URL https://doi.org/10.1080/14685240701767332.

[37] M. Marquillie, U. Ehrenstein, and J.-P. Laval, J. Fluid Mech. **681**, 205240 (2011), URL https://doi.org/10.1017/jfm.2011.193.

[38] G. Godard and M. Stanislas, Aerospace Sc. Tech. **10**, 181 (2006), ISSN 1270-9638, URL https://doi.org/10.1016/j.ast.2005.11.007.

[39] L. A. Schiavo, A. B. Jesus, J. L. Azevedo, and W. R. Wolf, Int. J. Heat and Fluid Flow **56**, 137 (2015), ISSN 0142-727X, URL https://doi.org/10.1016/j.ijheatfluidflow.2015.07.006.

[40] E. Dow and Q. Wang, in *52nd AIAA/ASME/ASCE/AHS/ASC Structures, structural dynamics and materials conference 19th AIAA/ASME/AHS adaptive structures conference 13t* (2011), p. 1762, URL https://doi.org/10.2514/6.2011-1762.

[41] P. S. Volpiani, R. F. Bernardini, and L. Franceschini, International Journal of Heat and Fluid Flow **97**, 109034 (2022), URL https://doi.org/10.1016/j.ijheatfluidflow.2022.109034.

[42] F. G. Schmitt, Comptes Rendus Mcanique **335**, 617 (2007), ISSN 1631-0721, URL https://doi.org/10.1016/j.crme.2007.08.004.

[43] L. Davidson and S. H. Peng, International Journal for Numerical Methods in Fluids **43**, 1003 (2003), URL https://doi.org/10.1002/fld.512.

[44] L. Temmerman, M. Had?iabdi?, M. Leschziner, and K. Hanjali?, International Journal of Heat and Fluid Flow **26**, 173 (2005), ISSN 0142-727X, URL https://doi.org/10.1016/j.ijheatfluidflow.2004.07.006.

[45] M. de la Llave Plata, V. Couaillier, and M.-C. le Pape, Computers & Fluids **176**, 320 (2018), ISSN 0045-7930, URL https://doi.org/10.1016/j.compfluid.2017.05.013.

[46] X. Gloerfelt and P. Cinnella, Flow, Turbulence and Combustion **103**, 55 (2019), ISSN 1573-1987, URL https://doi.org/10.1007/s10494-018-0005-5.

[47] H. Xiao, J.-L. Wu, S. Laizet, and L. Duan, Computers & Fluids **200**, 104431 (2020), ISSN 0045-7930, URL https://doi.org/10.1016/j.compfluid.2020.104431.

[48] F. Trias, A. Gorobets, and A. Oliva, Comput. and Fluids **123**, 87 (2015), ISSN 0045-7930, URL https://doi.org/10.1016/j.compfluid.2015.09.013.

[49] M. Zauner, V. Mons, O. Marquet, and B. Leclaire, Journal of Fluid Mechanics **937**, A38 (2022), URL https://doi.org/10.1017/jfm.2022.133.

[50] J. Ling, R. Jones, and J. Templeton, Journal of Computational Physics **318**, 22 (2016), URL https://doi.org/10.1016/

j.jcp.2016.05.003.
[51] M. Honnorat (2007), URL https://tel.archives-ouvertes.fr/tel-00273318.